UNIVERSITÀ DEGLI STUDI DI PADOVA

FACOLTÀ DI INGEGNERIA

CORSO MAGISTRALE IN INGEGNERIA
DELL'INNOVAZIONE DEL PRODOTTO

TESI DI LAUREA MAGISTRALE

CHARACTERIZATION AND MODELLING OF THE STRUCTURAL BATTERY ELECTROLYTE (SBE)

Relatore: Prof. Marino Quaresimin
Correlatore: Prof. Leif Asp

Laureando: Michele Spagnol

Matricola: 2013266

Anno accademico 2024/2025

Abstract

The transport sector faces several challenges when it comes to reducing its contribution to global warming and dependence on fossil fuels. This means that the transport sector needs to find alternative energy sources for its vehicles as well as to decrease the energy use in the use of life cycle. This can be achieved by turning from vehicles with conventional internal combustion engines to electric vehicles and reducing the vehicle weight. The latter can be accomplished by substituting conventional materials with lightweight materials such as carbon fiber composites. However, there are also solutions on how to combine these strategies where the energy is stored in the body, which will reduce the mass of the vehicle because of reduced battery size.

The thesis aimed to introduce the concept of structural battery composite materials, the characterization of the structural batteries electrolyte (SBE), and their possible devices. The worked areas addressed include carbon fiber electrodes, structural separators, multifunctional matrix materials, device architectures, and material functionalization. Fabrication and validation are also discussed. The thesis focuses on the characterization of SBE and the computational methodology for addressing mechanical stress arising and dimensional changes of the cell during electrochemical cycling, caused by time-dependent gradients in lithium-ion concentration distribution.

Acknowledgments

Having reached the end of this long journey, I feel from the bottom of my heart that I must thank many more than I can mention here.

My supervisor, Leif Asp: Thank you for your unwavering guidance, valuable insights, and endless patience throughout the entire research process. Your expertise and encouragement have been instrumental in shaping the direction of this work.

Ph.D. Ruben Tavano, Carl Larsson: Your mentorship, and scholarly insights have been indispensable throughout this research endeavor. Your commitment to academic excellence and your willingness to share your profound knowledge have left an indelible mark on the quality and depth of this thesis.
I extend my deepest appreciation for your dedication to the pursuit of knowledge and your generous investment of time and intellectual resources in shaping the scholarly trajectory of this work.

Mom and Dad: Your sacrifices, encouragement, and boundless love have been the bedrock of my existence. You have been my pillar of strength, believing in me even when I doubted myself. Your selflessness and sacrifices to ensure my success in this endeavor have not gone unnoticed, and I am profoundly grateful.

My brothers Raffaele, Leonardo, and Veronica: Simply thank you for the love you give me every day, you are the reason for my smile.

My extended family and friends: You have always been there when I needed you, you have always supported me and encouraged me even when I thought I was failing.
I especially want to say thank you to Nonna Maria and Filippo.

You have made me a better person.

CONTENTS

INTRODUCTION *6*

1.0 Multifunctional Materials **7**
1.0.1 Concept of Structural Power 7

1.1 State of the art for structural power batteries **9**
1.1.1 Introduction 9
1.2.2 The laminated structural batteries 10
1.2.3 Carbon fiber electrodes 12
1.2.4 Carbon Fiber Structure and How it can accommodate lithium 12

1.3 Structural battery architecture and fabrication **15**
1.4.1 Electrochemical properties of carbon fibers 17
1.4.2 Effect of lithiation on mechanical properties 19
1.4.3 Fiber electrode expansion during electrochemical cycling 20

1.5 Structural Battery Electrolytes (SBE) **21**
1.5.1 Multifunctional properties of the SBE 23

1.6 Background **24**

1.7 Scope **24**

EXPERIMENTAL SECTION *25*

2.1 SBE composition and manufacturing **25**
2.1.1 Specimens' preparation procedure 26
2.1.2 Tensile test samples 27
2.1.3 Compression test samples 30

2.2 Tensile test **31**
2.2.1 Measured properties 31
2.2.2 Speckle Pattern Analysis 33

2.3 Compression test **34**

2.4 Tensile test setup and methodology **35**

2.5 Compressive test and methodology **35**

2.6 SEM **36**

2.7 Shrinkage test **37**

THEORY *38*

3.1 Constitutive behavior of materials **38**
3.1.1 Elasticity 38
3.1.2 Hyperelasticity 39
3.1.3 Ogden model 40
3.1.4 Isotropic plasticity 41
3.1.5 Von Mises yield criteria 42

3.2 Raghava yield criteria **43**

3.3 FEM model **43**

3.3.1 Preliminaries 44
3.3.2. Constitutive model for the fiber domain, Ω_{cf} 45
3.3.3 Constitutive model for the structural battery electrolyte domain, Ω_{SBE} 47
RESULTS AND DISCUSSION 48
4.1 Tensile test results 48
4.2. Compression test results 52
4.3 Test considerations 55
4.4 SEM result 56
4.5 Shrinkage test 56
4.6. FEM results 57
CONCLUSIONS 64
FUTURE WORK 65
BIBLIOGRAPHY 66

INTRODUCTION

1.0 Multifunctional Materials

We are currently in an era where materials are experiencing a remarkable renaissance. Innovative material solutions are in the works to address the growing need for enhanced mobility, structural energy storage systems, and the advancement of well-being through healthcare monitoring and customization. These materials also serve as intelligent systems for proactive sensing and self-diagnosis, as well as the ability to adapt to local environments dynamically. Furthermore, they play a crucial role in enhancing product sustainability throughout their entire lifecycle via novel assembly and disassembly techniques. Such materials are commonly referred to as multifunctional.

1.0.1 Concept of Structural Power

Since the initial introduction of composites in the realm of transportation, the primary focus has been on enhancing their structural attributes, emphasizing qualities like compression strength and resistance to delamination. However, there has been a recent shift towards leveraging polymer composites for multifunctional purposes [1], [2]. This thesis centers on composite materials that serve both structural and electrical energy storage roles.

The concept of multifunctionality, as discussed by Gibson [1], comes into play. In numerous engineering applications, minimizing weight and/or volume stands as the primary design imperative. Traditionally, the approach has been to optimize individual subsystems, such as the power supply. However, addressing these subsystems in isolation yields only limited efficiency gains and often necessitates trade-offs in factors like durability, cost, and performance. A more holistic strategy involves the consideration of multifunctional structures [2], [3], [4], [5], [6], where the aim is to optimize the integration of diverse functionalities.

For example, in the context of the research presented here, thin-film batteries are embedded within composite laminates, creating what are essentially sandwich structures. This configuration not only capitalizes on enhanced structural performance through shape optimization but also allows these devices to operate effectively under low mechanical loads [2], [3], [4]. Nevertheless, this approach provides only modest reductions in mass and volume, and challenges such as delamination at the interface between the device and the composite material limit its potential. A comprehensive review of these composite materials can be found in [2].

This thesis focuses on an alternative approach, centered on the concept of crafting versatile materials [8–10] capable of fulfilling two or more functions concurrently. In the

scenario under consideration, polymer composites have the potential to bear mechanical loads while concurrently serving as reservoirs for electrical energy, as showcased in Reference. These materials are composed of multifunctional composite constituents that collaboratively provide structural and electrochemical energy storage functionalities. This undertaking presents a substantial dilemma because the ideal materials and configurations for these functions are often in conflict, frequently involving intersecting phenomena. Consequently, optimizing not only the components (fibers/electrodes and matrix/electrolyte) but also the composite structure is pivotal.

Nonetheless, the advantages of pioneering such materials are substantial, as they promise significant reductions in overall system weight and volume. This approach also opens up opportunities to integrate redundancy, accommodate potential cell malfunctions or in-service/impact damage, and customize mass distribution across a platform. Materials endowed with this array of functions hold profound implications for engineering design. They find applicability in a wide spectrum of fields, notably in aerospace, electric/hybrid ground transportation, and portable electronics, where the foremost challenges revolve around battery longevity and power management. Pioneering and inventive approaches to energy storage are indispensable to advance toward future environmentally friendly electric vehicles.

In the context of structural power composites, carbon fiber emerges as an appealing initial choice, given that carbon is conventionally utilized for both electrodes and as a high-performance structural reinforcement. Even though distinct forms of carbon have been traditionally used, the prospect of amalgamating these functions through suitable fiber modification becomes apparent. Similarly, polymers can serve as both a structural framework and an electrolyte; however, accomplishing these roles concurrently poses considerable technical hurdles. Furthermore, the layered configuration of structural composites mirrors that of numerous electrical energy storage devices, creating a compelling synergy

1.1 State of the art for structural power batteries

1.1.1 Introduction

The pursuit of structural battery composites has spanned over a decade. A substantial portion of research efforts has been directed towards developing structural battery elements, wherein slender, prismatic battery cells have been incorporated into structural components to impart an electrical storage capability to the structure [4], [5], [6].
As elaborated in the preceding section, this work explores an alternative paradigm for structural power, premised on the creation of genuinely multifunctional materials—a composite material wherein the individual components concurrently assume multiple roles. Pioneering strides in this direction were made by Wetzel and his team at the Army Research Laboratories in the United States [7]. They devised the inaugural structural battery composite material by employing diverse reinforcing materials for the electrodes, utilizing carbon fabric for the anode, (L_iF_ePo4) on a metal substrate for the cathode, and a glass weave separator, all embedded in a common polymer electrolyte matrix. This structural battery material exhibited promising mechanical characteristics but faced limitations in electrical insulation, preventing comprehensive electrical characterization. Subsequently, Liu and colleagues [8] designed a structural battery featuring short-fiber-reinforced electrodes and a solid polymer electrolyte matrix material. However, they encountered challenges in fabricating the electrodes with fiber reinforcement and identifying a solid-state electrolyte with adequate ionic conductivity. Consequently, they resorted to a robust gel electrolyte, which led to a working battery with suboptimal mechanical properties. Building upon this, Ekstedt and collaborators [9] successfully fashioned a functional structural battery employing a gel electrolyte fortified with a carbon fiber weave anode, a glass weave separator, and a LiFePO4/aluminum fiber weave cathode.
More recently, Asp and his team [10] introduced a groundbreaking concept for a structural battery, wherein individual carbon fibers served as the battery electrodes. They constructed the battery using approximately a thousand carbon fibers coated with a solid polymer electrolyte, embedded in a common cathode-doped matrix material. This innovative approach yielded a semi-structural battery with an energy density of 10 W h/kg. Furthermore, by enhancing the dispersion of the positive electrode, or cathode, an energy density of 175 W h/kg and a shear modulus of 1 GP_a became attainable.
Throughout these pioneering investigations into structural battery composite materials, various challenges warranting further examination have come to light. These issues are all linked, in one way or another, to the redox reactions occurring within the solid material. To actualize a structural battery material, it is imperative to achieve lithium-ion intercalation in the electrodes and facilitate lithium-ion migration between the electrodes, all while upholding the load-bearing capacity. This review provides a comprehensive overview of the research endeavors undertaken to realize the potential of structural batteries.

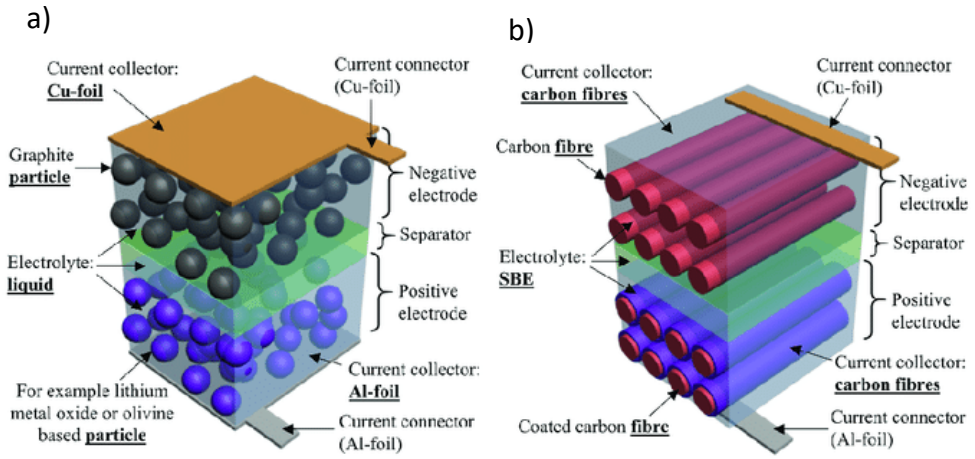

Figure 1.1: a) Schematic illustration of the conventional lithium-ion battery, b) Schematic illustration of the structural of the battery laminate.

1.2.2 The laminated structural batteries

Traditional methods for electrical energy storage encompass a range of devices, including batteries, supercapacitors, and dielectric capacitors. The principal factors under consideration are energy density, signifying the quantity of energy that can be stored, and power density, which denotes how rapidly the stored energy can be dispensed, as depicted in Figure 1.2. The idea of structural materials that can also serve as reservoirs for recoverable or transferrable energy is a broad one and encompasses a variety of multifunctional materials. Batteries, with their remarkable energy density, stand out as one of the most pivotal mechanisms for electrical energy storage. Hence, there is a keen interest in developing structural secondary, or rechargeable, battery materials. Batteries can be crafted from an array of chemical compositions, and among them, lithium-ion batteries have been a prime choice for pioneering innovative structural battery designs. Beyond their substantial specific energy, these batteries offer several advantages, including elevated operating voltage, minimal self-discharge, and the absence of a memory effect [11].

Both batteries and supercapacitors share the fundamental structure of two electrodes, an anode, and a cathode, separated by a permeable separator layer, all immersed in a lithium-ion-conductive electrolyte. Nevertheless, batteries present distinct challenges, primarily linked to the electrochemical redox reactions occurring within them, and these challenges also relate to the power and energy densities of the battery materials. Batteries operate by leveraging redox reactions to accumulate and transform chemical energy into electrical energy. In a typical battery, the reduction/oxidation reactions unfold as follows, where (MO_2) signifies a metal oxide [12]:

Anode reaction: $LiMO_2 \leftrightarrow Li_{1-x} + xLi^+ + xe$ (1.1)

Cathode reaction: $C + xLi^+ + xe^- \leftrightarrow Li_xC$ (1.2)

Total reaction: $LiMO_2 + C \leftrightarrow Li_xC + Li_{1-x}MO_2$ (1.3)

(→) Charge reaction
(←) Discharge reaction

Upon charging, the lithium-ion migrates from the cathode to the anode and coordinates with the carbon by accepting one electron. When discharging, the lithium-ion moves back into the cathode materials, and an electric current in the circuit results.

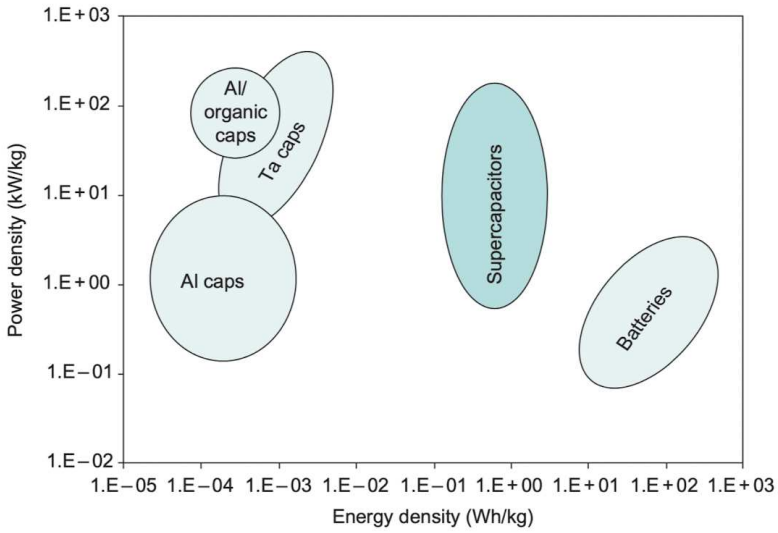

Figure 1.2: Plot showing the relationship between power and energy density for different conventional energy storage devices [13].

1.2.3 Carbon fiber electrodes

Various forms of graphitized carbons have been harnessed as the anode (negative electrode) in secondary lithium-ion batteries. Carbon is favored for its capacity to incorporate lithium ions at exceedingly low electrode potentials. The theoretical capacity of graphite, for instance, stands at 372 milliampere-hours per gram (mA h/g) [14]. Commercially accessible carbon fibers are typically manufactured for structural applications by emphasizing their remarkable specific stiffness and strength. These carbon fibers exhibit a microstructure characterized by a turbostratic graphitic arrangement. This specific carbonaceous microstructure enables a reversible Li-intercalation reaction [15]. With their combination of robust specific mechanical properties and the capability to incorporate lithium ions, carbon fibers become compelling candidates for reinforcing electrodes in structural battery composite materials. Consequently, evaluating and comprehending the electrochemical performance of carbon fibers is of paramount importance.

1.2.4 Carbon Fiber Structure and How it can accommodate lithium

Carbon fiber typically comes in the form of a continuous bundle known as a "tow," wound onto a reel. This tow is essentially a collection of numerous continuous individual carbon filaments bundled together and protected by an organic coating or sizing. It can be easily unwound from the reel for practical use. Each of these carbon filaments in the tow resembles a seamless cylinder with \a diameter ranging from 5 to 10 micrometers and is primarily composed of carbon. In earlier generations (e.g., T300, HTA, and AS4), these filaments had larger diameters of around 16 micrometers.

The atomic structure of carbon fiber closely resembles that of graphite, featuring sheets of carbon atoms arranged in a regular hexagonal pattern (known as graphene sheets). The key distinction lies in the way these sheets interconnect. In graphite, a crystalline material Figure 1.3, the sheets are neatly stacked parallel to each other in an orderly manner. The forces between these sheets are relatively weak van der Waals forces, which give graphite its characteristic soft and brittle nature.

The structure of carbon fiber varies depending on the precursor used to create it. Carbon fiber can be turbostratic or graphitic, or it may have a hybrid structure combining both graphitic and turbostratic components. Turbostratic carbon fiber exhibits sheets of carbon atoms randomly folded or crumpled together. Carbon fibers derived from polyacrylonitrile (PAN) exhibit a turbostratic structure, while those derived from mesophase pitch transform into a graphitic structure after undergoing heat treatment at temperatures exceeding 2200 °C. The process is detailed in Figure 1.3.

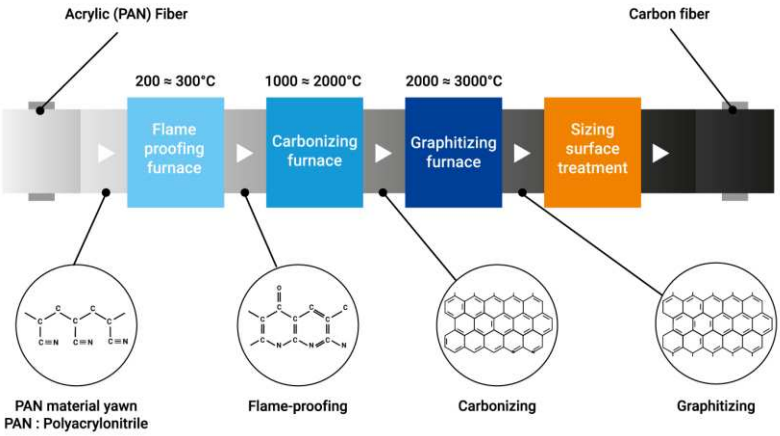

Figure 1.3: Process to obtain the carbon fiber (www.toray.com).

In general, carbon fibers (CFs) possess intricate microstructures, characterized as semi-crystalline and composed of graphite-like crystals arranged in a turbostratic manner, more or less oriented along the fiber axis. The microstructure of CFs can be significantly altered by selecting the precursor material and adjusting process parameters.
This variability allows for a wide spectrum of mechanical and physical properties.
The connection between microstructure and mechanical properties has been extensively understood.
Turbostratic carbon fibers, for example, exhibit notably high ultimate tensile strength.
On the other hand, heat-treated carbon fibers derived from mesophase pitch display a high Young's modulus, which translates to high stiffness or resistance to extension under a load, along with high thermal conductivity.
In the prior study, three types of PAN-based CFs were employed in structural batteries: IM fibers T800 and IMS65, and HM fiber M60J (as listed in Table 1.)[16]. The selection of IM and HM fibers was driven by the substantial distinction in their turbostratic graphitic structures. The HM fiber is notable for its higher lattice-dependent properties, such as tensile modulus, electrical conductivity, and thermal conductivity. However, it exhibits lower strength and strain to failure compared to the IM fibers. IMS65 and T800 IM fibers were chosen due to their highest electrochemical capacity, surpassing that of other CFs studied previously [14], [17], [18].

Table 1. Structural properties of the CFs from their respective data sheets (www.toraycf.com, www.tohotenax.com)

CF	T800	IMS65	M60J
Manufacturer	Toray[a]	Toho Tenax[b]	Toray
Type	IM	IM	HM
Sizing	40B	Unsized	50B
Tensile modulus (GPa)	294	290	588
Tensile strength (MPa)	5490	6000	3920
Strain to failure (%)	1.9	2.1	0.7
Electric resistivity ($\Omega \cdot$ cm)	$1.4 \cdot 10^{-3}$	$1.45 \cdot 10^{-3}$	$0.7 \cdot 10^{-3}$
Thermal conductivity (Cal/cm $\cdot$ s $\cdot$ °C)	0.0839	—	0.363
Carbon content (%)	96	(96)	>99
Final HTT range (°C)	1100–1600	1100–1600	1800–3000
Diameter (μm)	5	5	5
Density (g cm^{-3})	1.81	1.78	1.93

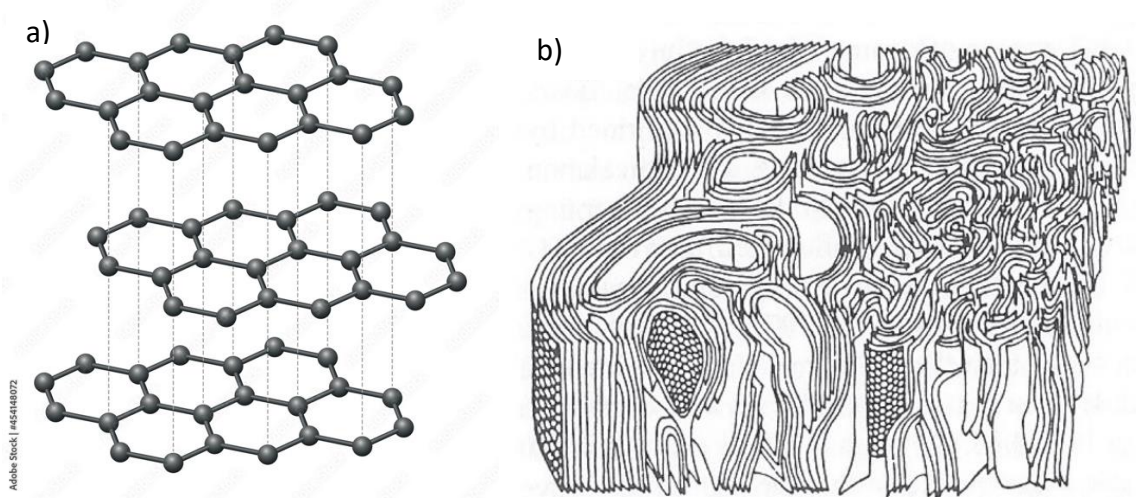

Figure 1.4: a) Graphite structure b) Turbostratic graphite structure [19].

It's been observed that the order of the structure defines different mechanical and electrical properties. The more the structure is disordered and more the carbon fiber is in favor of lithiation, so can accept more lithium atoms. The lithium predominantly is stored as cations, while the carbon host, here the CF, becomes negatively charged as it accepts electrons. This implies that the lithium ions are inserted between the graphite-like layers in the IM CFs and thus the mechanism resembles that of disordered carbons. Due to their disordered and open microstructure, these materials feature additional sites to graphite on the carbon lattice surfaces and edges to coordinate lithium ions.

Commencing with graphite, the capacity for lithium-ion storage experiences a diminishing trend as a function of crystallite thickness, particularly up to around 8 nanometers. This decrease is associated with heightened complications in accommodating lithium ions within the graphitic segments of the material, arising from greater microstructural disorder and turbostratic misalignment. This situation precisely elucidates why the M60J HM fiber exhibits a relatively low capacity. In contrast, when the disorder escalates even further, involving even smaller crystallite thicknesses and materials like glassy carbons and partially disordered carbons, the capacity surges. In these cases, lithium insertion and storage predominantly occur within the amorphous segments of the materials. Consequently, both IM fibers demonstrate substantially higher capacities compared to the HM fiber.

Likewise, the strength of the fibers is influenced by the size (length) of the crystallites, as it governs the defect size [20]. The tensile strength of the IM fibers stands at approximately 6000 MPa, while the HM fiber lingers close to 4000 MPa. This divergence in tensile strength aligns well with the variation in crystallite length, reported by Fredi and colleagues [16] to be approximately 20 Å for the IM fibers and 110 Å for the HM fiber.

The stiffness of the fibers, on the other hand, hinges on both the size and orientation of the crystallites. Notably, highly oriented and larger crystallites yield a higher stiffness[20].

1.3 Structural battery architecture and fabrication

The need for high energy and power density has immediate implications on the architectural designs of batteries and structural battery materials in particular. Starting with the obvious laminate layout, separating the positive and negative electrodes with an electrically insulating, lithium-ion conductive, separator layer (i.e., the traditional battery and composite laminate design). In the negative electrode (anode), the carbon fiber is the active electrode material, i.e., host for lithium, conducts electrons as a current collector, and carries mechanical load as reinforcement. A carbon fiber–based positive electrode (the cathode), where the carbon fibers are coated with lithium iron phosphate (LFP) particles. In this design, the carbon fiber has the role of electron conductor, reinforcement, and scaffold for the LFP coating. The two electrodes are separated by a glass fiber separator (Whatman GF/A) where the average thickness is 185μm and the stack is impregnated with a structural battery electrolyte (SBE). The SBE is a multifunctional composite matrix material with the tasks to transfer mechanical loads between fibers as well as between layers, i.e., plies of fibers, and to transport lithium ions, i.e., be ionically conductive. The utilized SBE is a bi-continuous multiphase material. Mechanical performance is provided by a porous glassy polymer. Ionic conductivity is achieved as the pore volume in the glassy polymer is occupied by an ionically conductive solution [21]. An illustrative overview of the structural battery composite full-cell manufacture is shown in Figure 1.5 [22]. All the first part of fabrication is made inside a glovebox to avoid any contact with air and moisture that could react with the components of the battery. The negative electrode was made from a CF spread tow and the positive electrode is an electrode obtained via electrophoretic deposition (EPD) of LiFePO4 (LFP), carbon black, and polyvinylidene fluoride (PVDF) onto carbon fibers. A copper foil current collector is adhered to the CF negative electrode using silver conductive paint. An aluminum current collector is placed on the CF positive electrode and between the two electrodes is placed a glass fiber separator (Whatman GF/A) to ensure that the electrodes don’t come in direct contact (to avoid short circuits). The battery cell stack is placed inside a pouch laminate bag to protect the electrochemical cell from air and moisture. The battery cell is then impregnated with an SBE mixture before the pouch bag is vacuum heat-sealed. To achieve a homogeneous solution, the SBE mixture is stirred using a vortex before it is added to the battery cell. Once the pouch bag is vacuum heat sealed, it's transferred to a preheated oven outside the glovebox and thermally cured at 90°C for 60 min. During thermal curing, pressure is applied to the cells using clamps.

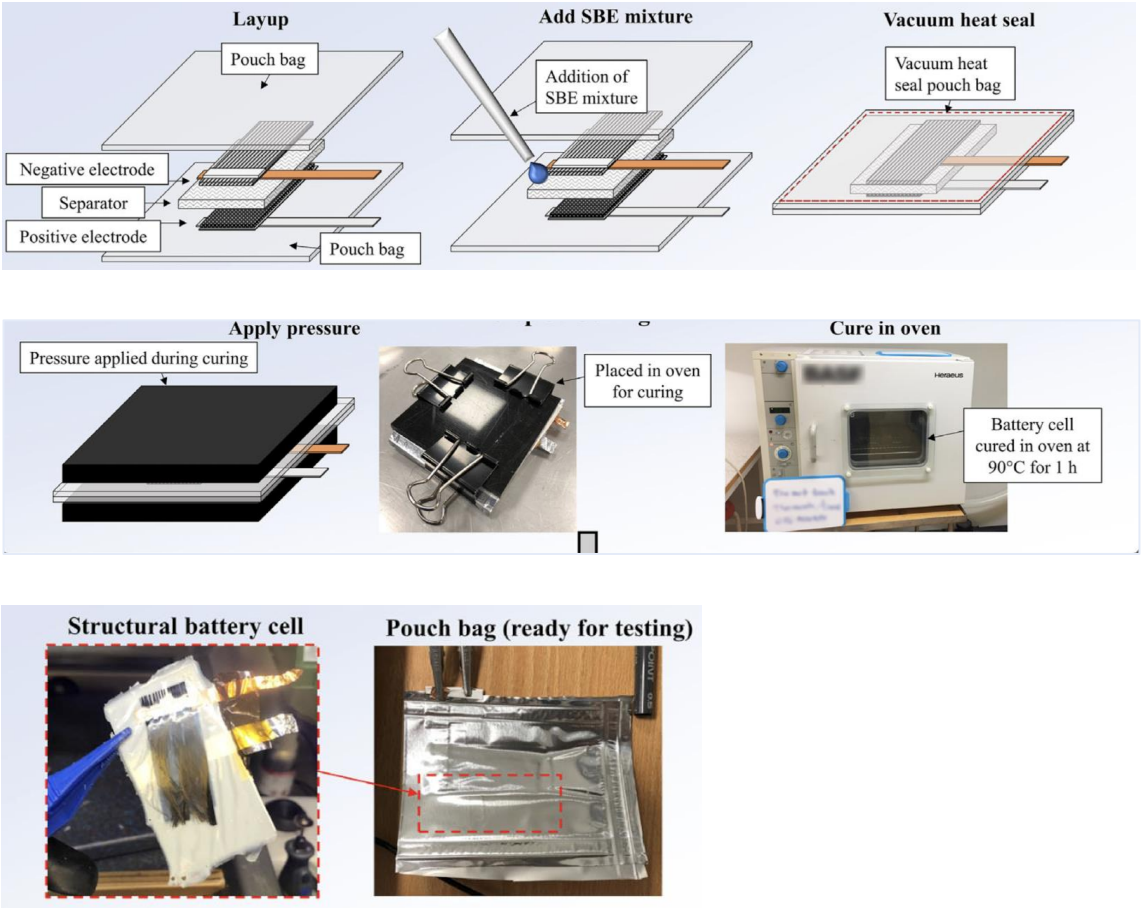

Figure 1.5: Structural battery composite fabrication steps [22].

1.4 Carbon fiber as a negative electrode in structural battery composites

In the development of structural battery composites, carbon fibers are tasked with a dual role, requiring them to simultaneously bear mechanical loads and function as active battery electrodes. In the latter capacity, these carbon fibers must possess the capability to store ions within their microstructure. This process involves the insertion of ions, such as lithium ions, into the fiber during the charging phase (lithiation) and their removal during discharge (delithiation). This dual role raises critical questions regarding the behavior of the carbon fiber itself.

One of these questions pertains to the potential influence of mechanical loads on the processes of lithiation and delithiation. In other words, does the application of mechanical stress impact how these ions are absorbed and released within the fiber? Furthermore, it's essential to explore the changes that occur within the fiber as lithium ions occupy space within its microstructure and assess whether these alterations have any discernible effects on the mechanical properties of the fiber.

1.4.1 Electrochemical properties of carbon fibers

In the research conducted by Snyder and colleagues in their study [23], they identified that carbon fiber electrodes derived from polyacrylonitrile (PAN)-based fibers with high and intermediate modulus exhibited the most optimal balance between specific capacity and tensile strength. To evaluate the electrochemical performance of these carbon fibers, the researchers employed specialized pouch cell batteries. These batteries featured a negative electrode composed of a carbon fiber tow and a counter electrode made of lithium foil, separated by a glass fiber fabric. Galvanostatic cycling was carried out within the voltage range of 0.002 to 1.5 V versus Li/Li+ for ten cycles, with a current corresponding to 100 mA/g of carbon fiber.

It was noted that there was a decline in electromechanical capacity after the initial lithiation/delithiation cycle, as depicted in Figure 1.5 [13] for the IMS65 carbon fiber tow. The figure illustrates capacity plotted against electrode potential. Capacity represents the energy that a battery can deliver, while electrode potential signifies the electromotive force of a galvanic cell formed between a standard reference electrode and the electrode under evaluation. As per convention, the reference electrode is the standard hydrogen electrode (SHE), which is defined to have a potential of zero volts.

This capacity reduction following the first charging cycle is a common occurrence in lithium-ion batteries and is attributed to the formation of an exceedingly thin passivation layer known as the solid-electrolyte interphase (SEI). This SEI formation is a consequence of the electrolyte decomposition at the carbon electrode surfaces during the initial charge cycle, as elucidated in reference [24].

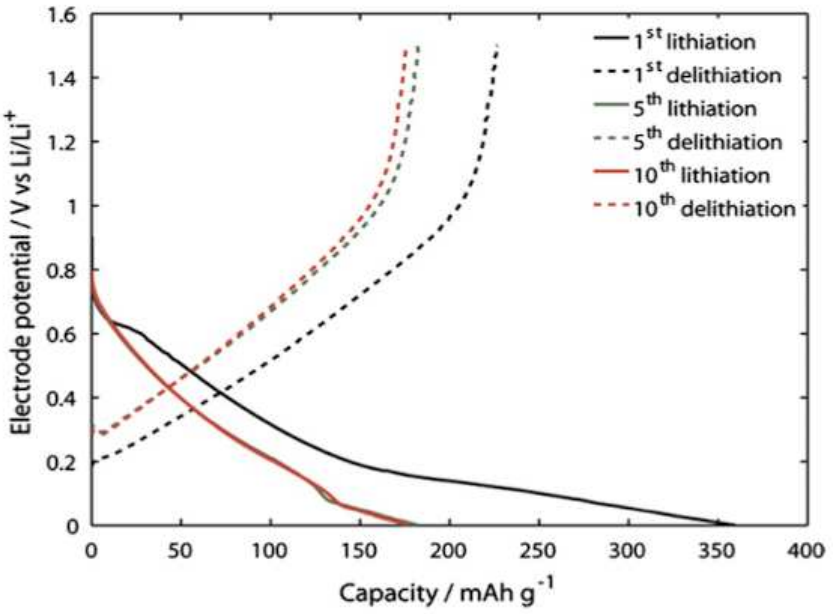

Figure 1.6: Lithiation/delithiation curves at 100 mA g1 for the 1st and the 10th cycle for unsized IMS65 [40].

Figure 1.7 [22] presents various electrochemical performance metrics. In Figure 1.6 a), we can observe the energy density of a cell at different true C rates. The data reveal a modest decline in capacity, signifying a reasonably stable energy density at the investigated C-rates.
Moving on to Figure 1.5 b) displays the capacity retention of a structural battery cell that employed a Whatman GF/A separator during 500 cycles at an approximate 1C (true C-rate). After these 500 cycles, the capacity retention stands at 40%. This outcome indicates that the tested structural battery cell exhibits subpar capacity retention, which is a measure of a battery's ability to preserve stored energy during a prolonged period of open-circuit rest.
Nevertheless, despite the suboptimal capacity retention, the battery maintains a high Coulombic efficiency, denoting efficient energy conversion and delivery. It's important to note that the electrodes used in structural batteries closely resemble those found in conventional batteries. Therefore, the primary factors contributing to the reduced capacity retention in structural batteries can be ascribed to the Solid Battery Electrolyte (SBE) and its impact on ionic conductivity.
The SBE combines salts that exhibit lower conductivity when compared to conventional Li-ion battery salts. Moreover, the unique morphology of the SBE, where the electrolyte is confined within the polymer's interconnected pores, directly influences ionic conductivity, as discussed in reference [25].

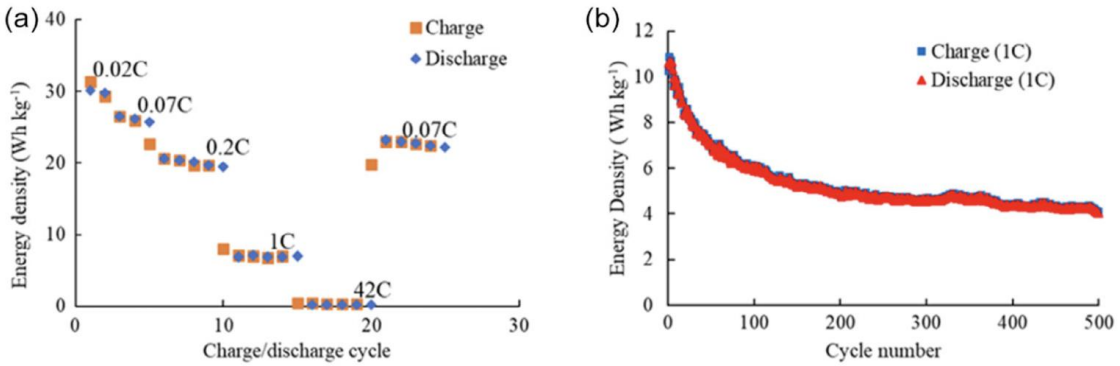

Figure 1.7: Results from electrochemical characterization based on the total weight of the battery cell. left) Voltage profile at different C rates. right) Energy density at different [22].

An additional trial was carried out to assess the electrochemical characteristics of a structural battery composite employing a Whatman GF/A separator, as depicted in Figure 1.6 a). This figure illustrates the characteristic charge and discharge voltage patterns of the structural battery cells during galvanostatic cycling at various C rates. The voltage profiles manifest a consistent charge and discharge process at these diverse C rates, indicative of a well-balanced cell performance.
Simultaneously, we can observe a reduction in specific capacity as the C rates increase. This decrease is attributed to the fact that higher rates lead to accelerated capacity deterioration, primarily resulting from the mechanical wear and tear inflicted on the active particles.

1.4.2 Effect of lithiation on mechanical properties

In a study conducted by Jacques and colleagues in 2012 [24], they investigated the impact of lithium insertion on the mechanical properties of carbon fibers. The specimens used in the experiments featured T800 and IMS65 fiber tows. These specimens underwent cycling within a pouch cell at a 1 C rate for a duration of up to 1000 cycles. The mechanical properties, including longitudinal stiffness and strength, were assessed at intervals during the cycling process.
The results of this study indicated that lithium insertion didn't appear to significantly affect the stiffness of the fibers. However, the tensile strength did exhibit a reduction upon lithiation, albeit some of this reduction was recovered as the fibers underwent delithiation. This observation suggests that some amount of lithium remains trapped within the carbon fibers even after discharging.
In another study by Jacques and colleagues in 2014 [26] replicated a similar experiment, but this time, stiffness and strength were measured in relation to the capacity, which corresponds to the amount of lithium inserted into the fibers. The findings revealed that stiffness remained relatively constant with increasing capacity. However, at very slow charge rates, substantial reductions in ultimate tensile strength (UTS) were observed. In other words, at high capacities (slow charge rates), the reduction in UTS was more pronounced compared to what was observed at low capacities (high charge rates) [26].
Contrary to this, after the initial cycle, each lithiation event caused a drop in the ultimate tensile load, which was subsequently recovered during delithiation. This drop in tensile load can be attributed to the presence of lithium ions inserted between the graphitic layers of the fiber, potentially causing the layers to separate and affect their lateral bonding. Additionally, the elongation of the fiber in the longitudinal direction, as measured in reference [27] during lithium-ion intercalation, could indicate that a deformation of the fiber's microstructure during lithium-ion intercalation contributes to the loss in strength. During delithiation, the removal of lithium ions from the fiber might release this internal deformation, allowing for the recovery of strength.
In summary, these findings suggest that the inserted lithium ions create elastic strains within the carbon fiber, which results in the fiber becoming pre-stressed in tension, rather than experiencing irreversible damage.

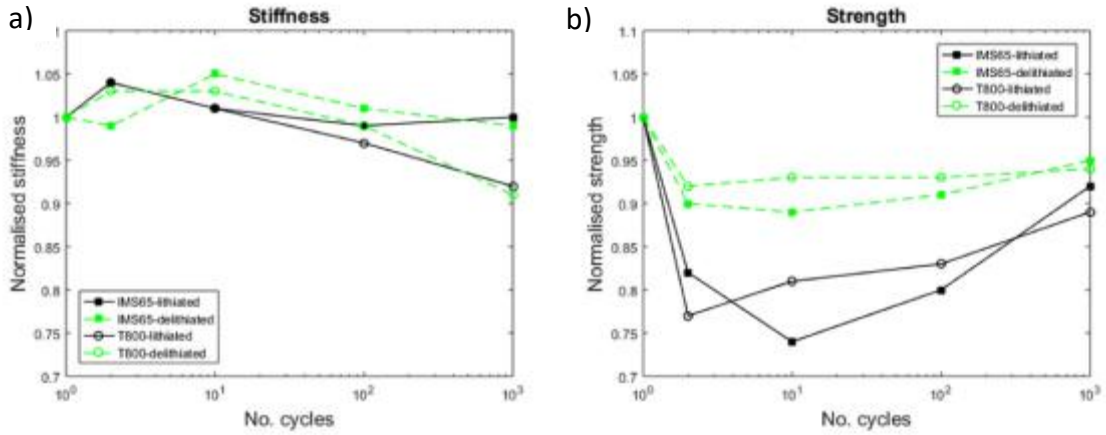

Figure 1.8: a) Stiffness, b) strength of carbon fiber after electrochemical cycling reprinted from (Jacques et al (2012) [28].

1.4.3 Fiber electrode expansion during electrochemical cycling

As previously mentioned, the process of lithium intercalation within carbon fibers leads to their expansion, resulting in a variety of consequences in both mechanical and electrochemical aspects. The overall elongation of the fibers in the longitudinal direction is approximately 0.85%, of which about 0.8% is reversible. Consequently, the remaining 0.05% represents an irreversible expansion, attributed to factors such as trapped Li-ions and the formation of the solid-electrolyte interphase (SEI). Notably, this irreversible expansion is predominantly prominent during the initial charge and discharge cycle.
The stretching of the electrode can induce a warping or twisting of the battery cell during its operation unless this mode of deformation is mitigated. Furthermore, uneven lithiation of the fibers may lead to warping or twisting of the CF-SBE electrode. Therefore, to accurately anticipate and optimize the collective electro-chemo-mechanical response of battery cells utilizing CF-SBE electrodes, it is imperative to meticulously account for electrode expansion in the design phase. This consideration is crucial for averting any potential damage, degradation, or undesirable warping and deformation of the battery cell.

1.5 Structural Battery Electrolytes (SBE)

A significant challenge in the development of structural battery electrolytes (SBE) lies in creating a composite matrix that can effectively facilitate lithium-ion conduction while also bearing mechanical loads imposed by the carbon fibers. These two essential properties often run counter to each other. In recent advancements in structural batteries, a bi-continuous polymer structural battery electrolyte (SBE) has been employed. This SBE's porous structure is established through a polymerization-induced phase separation (PIPS) reaction. The solid polymer backbone ensures the overall structural integrity, while the liquid electrolyte, situated within the porous network, facilitates the transport of lithium ions. This particular SBE structure offers a well-balanced compromise, boasting a commendable ionic conductivity (approximately $\sim 2 \cdot 10^{-4}\, Scm^{-1}$) and favorable mechanical properties, characterized by an elastic modulus of 540 MPa.
In a recent study by Duan and colleagues in 2023, a combined approach employing focused ion beam and scanning electron microscopy (FIB-SEM) was harnessed to obtain high-resolution 3D data. High-quality images were acquired through FIB-SEM, enabling the creation of 3D models representing the polymer and pore phases of the SBE. These models were subsequently utilized to scrutinize pore size distribution and tortuosity. Furthermore, the reconstructed 3D model played a pivotal role in the development of finite element models for both phases. As illustrated in Figure 1.9 [25], 3D models of the SBE were meticulously reconstructed, shedding light on the structural intricacies of this critical component.

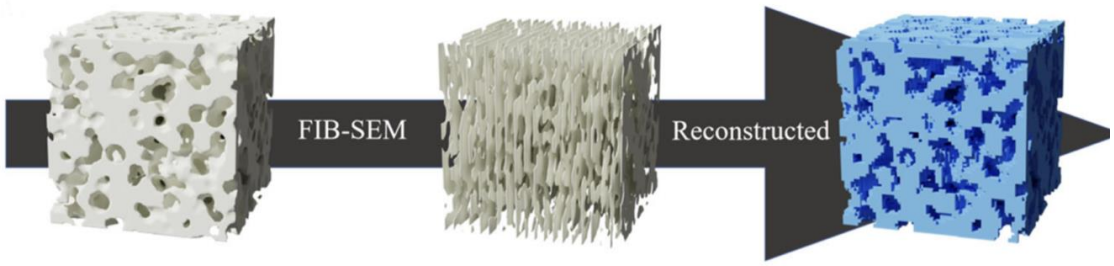

Figure 1.9: Illustration of 3D reconstruction of the SBE model [25].

Utilizing this method, researchers calculate the porosity within the structural battery electrolyte (SBE) by analyzing the volume ratio between the liquid electrolyte and monomer in the SBE mixture before it undergoes curing. It's important to consider that roughly 8-10% of the liquid electrolyte is absorbed into the bulk polymer, as determined through nuclear magnetic resonance. The resulting porosity falls within the range of 37-38%, and you can observe this in Figure 1.10 [25].

To construct the 3D model of the polymer, the research team removes the pixels representing the pores, followed by transforming the polymer pixels into voxels, each with a thickness of 20 nm. Unfortunately, this method doesn't identify pores smaller than 20 nm. Nevertheless, the influence of these minuscule pores on the material's elastic properties is considered negligible. In cases where a significant number of these smaller pores exist, there's a possibility that the volume of the interconnected larger pores, and subsequently the ionic conductivity, could be overestimated. Despite the appearance of some isolated pores on the surface of the 3D model, 99.3% of the pores are spatially interconnected. These isolated surface pores likely connect to other pores outside the reconstructed volume. The measurements reveal a diameter of 180 nm for the polymer segments and 160 nm for the pores.
This unique structural configuration hinders lithium ions from following a direct and linear path when moving through the porous SBE. Research indicates that the geodesic tortuosity, which characterizes the winding path a particle must traverse, is similar in all three spatial directions, confirming the SBE's isotropic nature. An average geodesic tortuosity of 1.8 is determined, implying that a lithium particle needs to traverse a distance 1.8 times longer to reach the carbon fibers due to the complex path created by the porous structure.

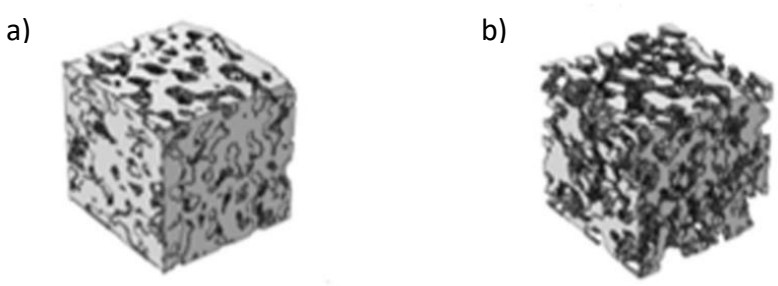

Figure 1.10: a) 3D reconstructed model of the polymer, b) Liquid electrolyte on the right [25]

1.5.1 Multifunctional properties of the SBE

Dynamic mechanical analysis (DMA) and electrochemical impedance spectroscopy (EIS) were carried out to evaluate the storage modulus and ionic conductivity, respectively. The bulk polymer exhibited a measured elastic modulus of 2167 MPa, while the liquid electrolyte demonstrated an ionic conductivity of $4.35 mS\ m^{-1}$. These obtained property values served as the initial parameters for the finite element method (FEM) analyses, which relied on the principles of linear elasticity and linear Fickian diffusion. Moreover, a Poisson's ratio of 0.33 was enforced for the polymer phase.
Within the framework of the FEM analyses, it was postulated that the elastic modulus exclusively pertains to the polymer phase, and the ionic conductivity is solely attributed to the liquid phase. Multiple FEM simulations revealed a clear and inverse relationship between the elastic modulus and ionic conductivity concerning the ratio of the solid-to-liquid phase, as illustrated in Figure 1.11 [25].

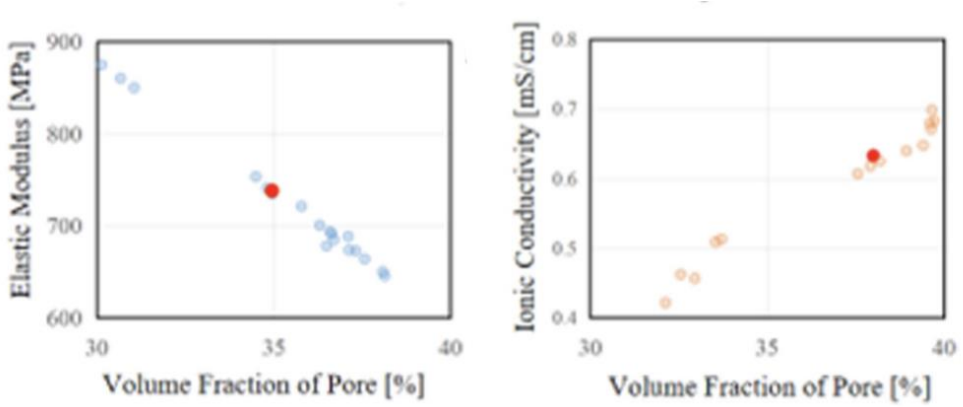

Figure 1.11: FEM simulation for the elastic modulus and ionic conductivity concerning the pore fraction. The red dot represents the final average result [25].

1.6 Background

The electrochemical cycling process, involving the insertion and extraction of lithium ions within the microstructure of carbon fibers, introduces a level of uncertainty regarding its impact on the material's stress state. The stress tension arises primarily from the axial expansion and contraction, as documented by Jacques et al. in a related study [28]. The resultant volume changes can give rise to high-stress areas, particularly concerning the polymeric matrix, which experiences variations in volume due to fiber-induced compression.
To address these potential challenges, a comprehensive understanding of how all the components within the structural battery work together is essential. This research is specifically dedicated to unraveling the mechanical properties and behavior of the structural battery electrolyte, shedding light on the interactions and behaviors of the various components involved in this multifunctional system.

1.7 Scope

The primary objective of this research is to gain insights into the behavior of the structural battery electrolyte (SBE). The main purpose of this research is to describe the mechanical behavior of SBE by defining reference values. These values, such as the elastic modulus and rupture stress, will be determined through tensile and compression tests. Once these essential values are defined to characterize the material behavior, the model already developed by researchers at Chalmers University will be considered to assess how SBE behaves during a lithiation process. Furthermore, yielding criteria will be established to understand how the polymer reacts to the stress levels applied during the lithiation process of carbon fibers.

EXPERIMENTAL SECTION

2.1 SBE composition and manufacturing

The Structural Battery Electrolyte (SBE) is a complex composite matrix material that serves a dual purpose. It first acts as a medium for transmitting mechanical stresses between individual fibers and layers (plies) of fibers, effectively distributing these loads. Simultaneously, it facilitates the transport of lithium ions, thereby exhibiting ionic conductivity. Its mechanical strength is achieved through the presence of a porous, amorphous polymer, while its ionic conduction is established by filling the pores within the glassy polymer with an ionically conductive solution.
As mentioned earlier, the SBE plays a crucial and specific role in Structural Batteries, and its composition involves mixing the following components in a 50:50 weight ratio:

- Liquid electrolyte solution made from a mixture of $LiBoB$ and $LiTf$ at concentrations of 0.4 and 0.6M, respectively, in EC:PC 1:1 weight.

- Monomer bisphenol A ethoxylate dimethacrylate and thermal initiator AIBN (with 1% of monomer in weight).

As demonstrated in previous studies, it is crucial to prevent the polymer from coming into contact with air and humidity. Exposure to air can lead to a reaction with the moisture in the atmosphere, which inhibits the polymerization process. To address this concern, the SBE manufacturing process takes place within a glove box where the normal atmosphere is replaced with Argon gas.
Once all the components are thoroughly mixed to achieve a uniform solution, the SBE mixture is agitated using a vortex. Following this step, the solution is transferred to an oven for the curing process. To maintain the integrity of the SBE and prevent exposure to air and moisture, the transfer and curing processes are carried out with the SBE sealed inside a pouch within the glove box.
The curing process is employed to thermally activate the AIBN initiator. The SBE is thermally cured at 90°C for 45 minutes, resulting in a ready-to-use polymer.

2.1.1 Specimens' preparation procedure

To get the specimens for the test, various attempts are being made. Since no one has ever tested this material before, it was important to create a repeatable procedure in order to create a guideline for future work. Follow the guidelines of the procedure and the explanation of the various measures.

The fabrication of an SBE involves a complex process that utilizes a controlled-atmosphere chamber, known as a glovebox. This chamber consists of a hermetically sealed metal enclosure within which a defined gas pressure and composition can be maintained.
For SBE fabrication, an oxygen- and moisture-free environment is essential. Exposure to these atmospheric agents can degrade the polymer used in SBE construction.
The SBE fabrication process comprises two main stages:

- Component Mixing: The first stage involves mixing the various SBE components in the right ratio
- Polymer Curing: The second stage involves polymer curing, transforming it from a liquid to a solid state. Curing takes place in an oven at 90 °C for 60 minutes.

The challenge of this stage lies in the oven's location outside the glovebox, in another room. This means the liquid polymer, still sensitive to oxygen and moisture, must be transported from its controlled environment to an open environment.

To address this, the liquid polymer is sealed within pouch bags using a sealing machine inside the glovebox. This ensures the sealed SBE within the bag maintains the same controlled atmosphere and can be easily transported to the curing oven. Once the curing phase is complete, the polymer has solidified and can be exposed to the external environment because the cross-linking process has been completed, and the presence of humidity in the air no longer affects its structure.

2.1.2 Tensile test samples

To fully evaluate their mechanical properties, tensile testing is employed. However, fabricating dog-bone-shaped specimens suitable for tensile testing can be a challenging task.
The process involves creating polymer sheets within glass molds, which are later cut to the desired shape using water jet cutting. The decision to use polymer sheets deposited in glass molds was based on several factors:

- The SBE cannot be deposited in molds obtained through 3D printing, as their porosity allows the polymer to infiltrate, leading to it getting stuck to the mold after curing.

- The need for molds to have tall walls to facilitate handling when sealing them inside pouch bags and subsequently transporting them from the glovebox to the oven for curing. This is done to prevent spilling during various handling processes. Figure 2.1 below illustrates this concept.

- Gas generation during the curing process. It has been observed that gas is generated during the polymerization reactions. Since these gases are lighter than the polymer, they attempt to evaporate, leading to the formation of air bubbles if there is no space to accommodate the gas generated during the reaction. This can compromise the final structure, making it non-uniform and unsuitable for testing. The issue has been resolved by utilizing the tall side walls of the mold, creating an air gap between the mold and the pouch bag. The image below represents the described concept.

- The choice of a glass mold is due to the fact that SBE does not adhere to it, making its removal easier after the curing process.

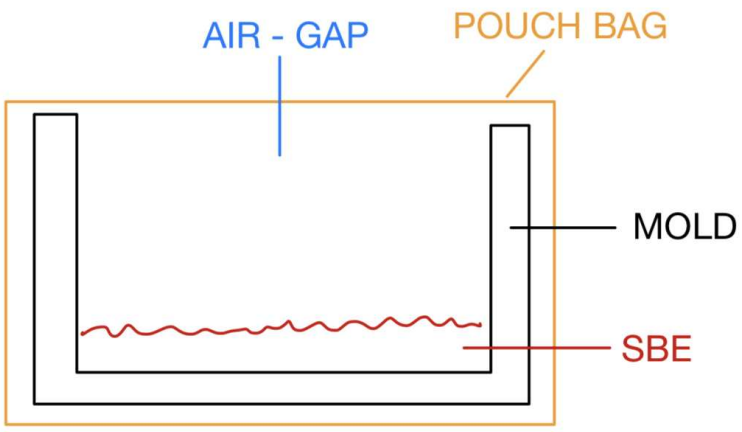

Figure 2.1: Mold schematization.

With the reasons for choosing this method for obtaining dog bone-shaped specimens, a guideline for achieving the specimens in a repeatable and standardized manner is established:

1. Mixing of SBE Components: Carefully weigh the SBE components in the specified ratios to ensure the desired electrochemical properties.

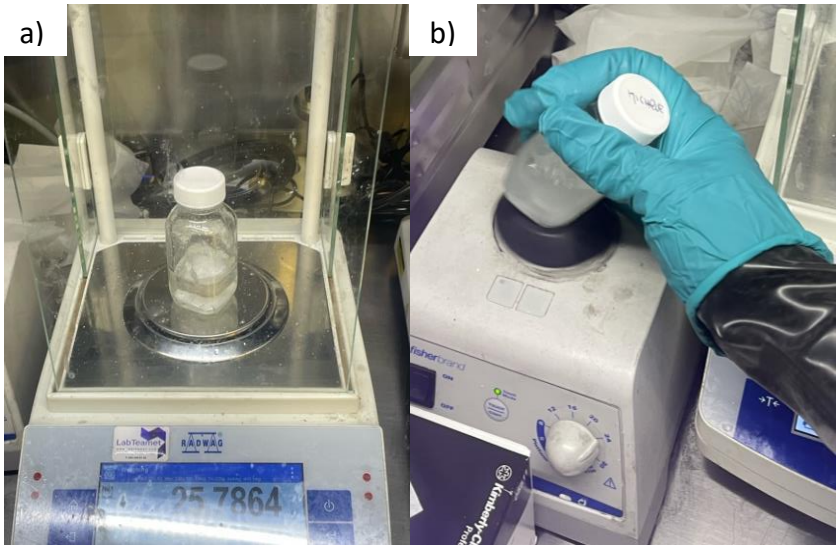

Figure 2.2: a) Weighing process b) mixing process through a vortex.

2. Preparation of Glass Molds: Inspect the glass molds for any cracks or imperfections that could compromise the specimen's integrity. Clean the molds to remove any impurities.

3. Polymer Deposition: Accurately mix the SBE components and deposit the mixed solution into the glass mold.

4. Mold Sealing: Seal the glass mold within a pouch bag using a sealer. This maintains a controlled atmosphere and prevents contamination during transportation to the curing oven.

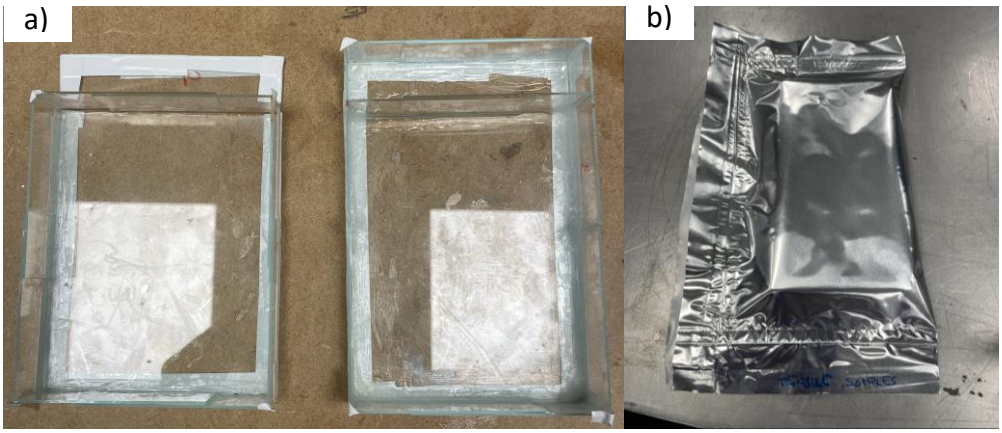

Figure 2.3: a) Glass mold used for the polymer deposition b) Mold sealed inside the pouch bag.

5. Curing in Oven: Place the sealed mold in an oven preheated at 90°C for the curing temperature. Maintain the curing temperature for 45 minutes, allowing the polymer to transform from liquid to solid.

6. Specimen Extraction: Carefully open the pouch bag and remove the cured SBE specimen from the glass mold. Avoid excessive handling to prevent specimen deformation.

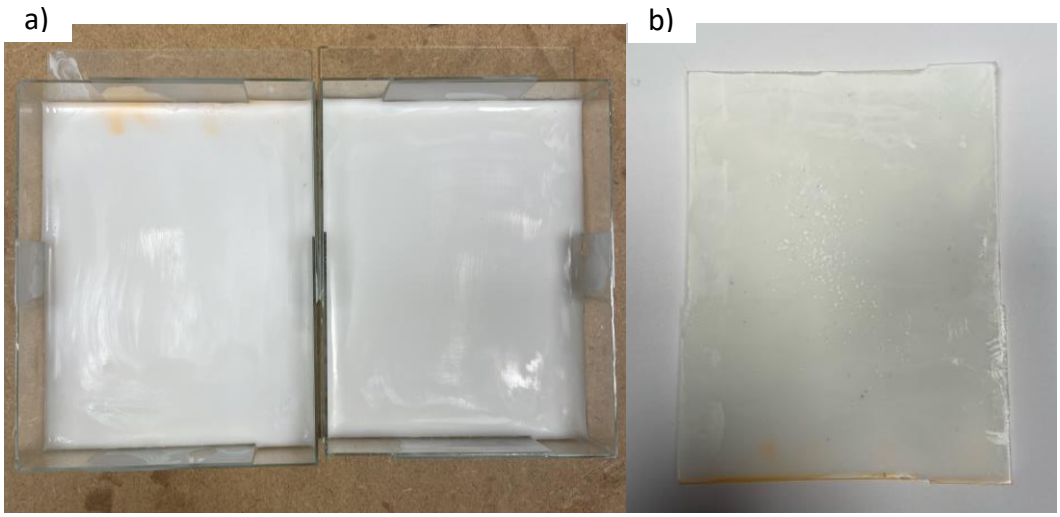

Figure 2.3: a) Polymer sheet after curing inside the mold b) Final polymer sheet.

7. Waterjet Cutting: Cut the cured SBE specimen into dog-bone-shaped tensile test specimens using a waterjet cutter. The waterjet cutting ensures precise dimensions and shape integrity, ensuring accurate testing results.

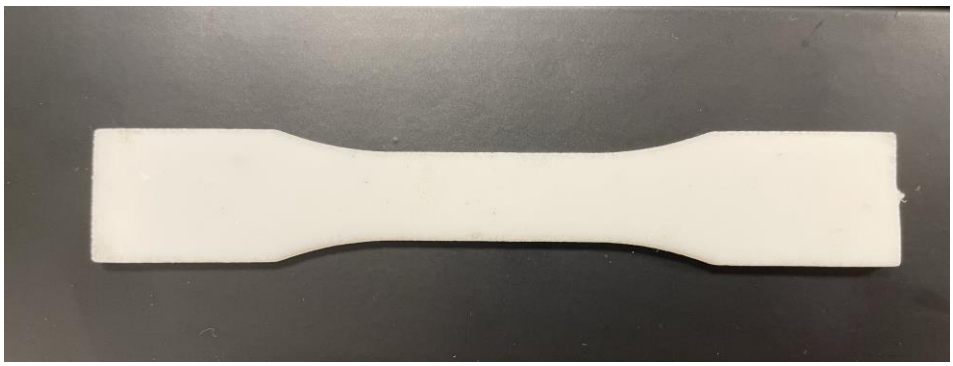
Figure 2.4: Dog bone specimen.

2.1.3 Compression test samples

The creation of the cylinders was simpler than the production of dog-shaped samples for the tensile test also because the knowledge derived from the production of tensile samples was exploited. To obtain the cylindrical shape, syringes were used as molds and capsules for atmosphere maintenance.
The manufacturing followed the following steps:

1. Mixing of SBE components: Carefully weigh the SBE components in the specified ratios to ensure the desired electrochemical properties.

2. Injection of the polymer into the syringe: Insert the polymer into the syringe and close the upper end of the syringe with polymeric rubber to preserve the controlled atmosphere.

3. Oven curing: Bake in the oven for 60 minutes at 90°C, allowing the polymer to transform from liquid to solid.

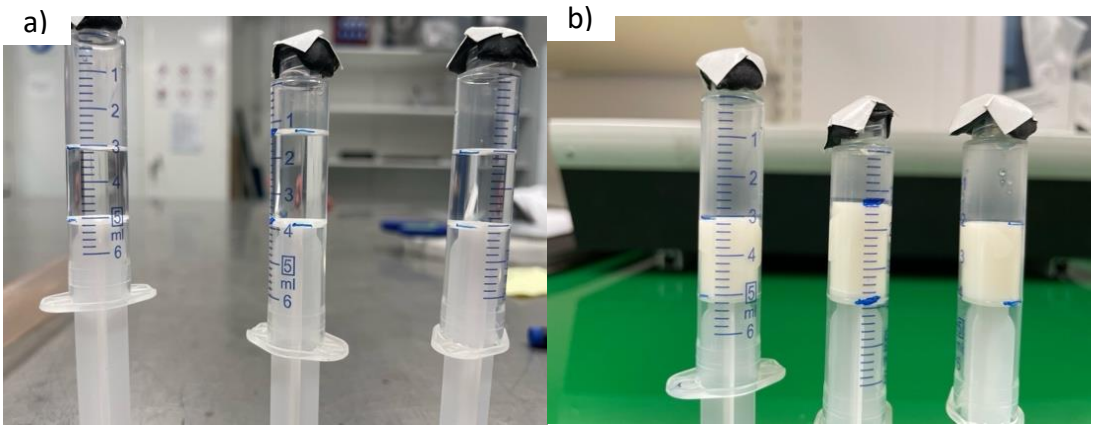

Figure 2.5: a) SBE pre-cure, b) SBE after cure.

4. Specimen Extraction: Extract the cylinders from the syringes.

5. Final polishing treatment: Apply a final polishing treatment to obtain flat surfaces at the ends.


Figure 2.6: Specimens after polishing treatment

2.2 Tensile test

A tensile test is a destructive test method used to measure the tensile strength and other properties of materials. Tensile testing is one of the most common mechanical testing techniques and is used in a wide range of industries, including aerospace, automotive, construction, and manufacturing.
To perform a tensile test, a specimen of the material to be tested is prepared to a specific shape and size, in this case following the ASTM D638-14, specific for polymer. The specimen is then gripped at each end and placed in a tensile testing machine. The machine applies a force to the specimen, pulling it in tension. The force and elongation of the specimen are measured during the test. This test aims to get the curve stress-strain which describes the material's behavior under load.

Definitions

Stress (σ): The force applied per unit area and is calculated as ($\sigma = \frac{F}{A}[MPa]$), where ($F$) is the force applied and (A) is the original cross-sectional area of the specimen.

Strain (ε): The measure of deformation and is calculated as ($\varepsilon = \frac{\Delta L}{L_0}$), where ($\Delta L$) is the change in length and (L_0) is the original length of the specimen.

2.2.1 Measured properties

Several material properties are measured, including:

- Ultimate Tensile Strength (UTS): The maximum stress that the material can withstand before it breaks.
- Yield Point**:** The point at which a material begins to deform plastically (if it is available).
- Elongation: The amount of plastic deformation that the material can undergo before it breaks.
- Modulus of elasticity: The stiffness of the material.
- Poisson's ratio (υ): is a material property that relates the lateral strain to the axial strain in a material undergoing deformation.

Poisson's ratio is determined by the following formula:

$$\upsilon = -\frac{Lateral\ Strain}{Axial\ Strain}$$

Elastic Modulus (Young's Modulus) is determined as:

$$E = \frac{\sigma}{\varepsilon}\ [MPa]$$

The rest of the properties can be obtained from the curve stress-strain.
The dimensions of the specimens are provided in the following figure, Figure 2.7.

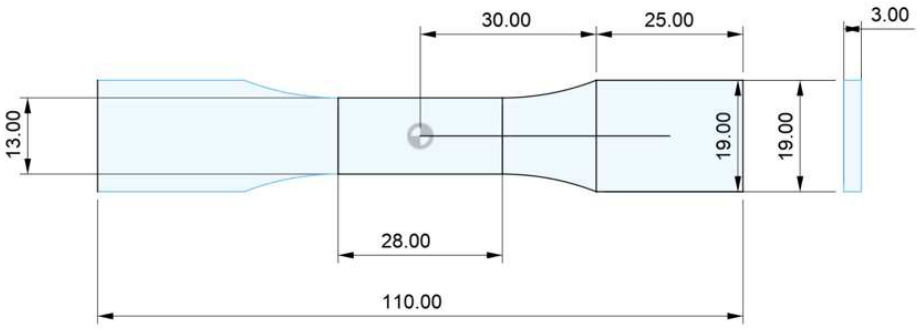

Figure 2.7: Dimension of the specimens according to ASTM D638-14

In this case, due to the slippery nature of the specimens, the elongation measurement is performed via speckle pattern analysis and not with an extensometer.

2.2.2 Speckle Pattern Analysis

Speckle pattern analysis is a technique commonly used in optical methods, particularly in digital image correlation (DIC), for measuring material deformation and strain. The technique involves applying a random speckle pattern to the surface of a specimen, which serves as a unique and identifiable surface texture. As the material deforms, the movement and deformation of the speckle pattern are tracked and analyzed to determine displacement and strain.

- Speckle Patterns**:**

A speckle pattern consists of a random distribution of small, high-contrast spots or grains on the surface of a material. These spots are typically applied using techniques such as painting the surface with a speckle paint or using a laser to create a speckle pattern. The randomness and contrast of the speckle pattern are crucial for accurate tracking during deformation.

- Deformation Tracking**:**

When the material undergoes deformation, the speckle pattern deforms along with it. The movement of individual speckles or the pattern as a whole is tracked using optical methods, such as cameras or laser-based systems. The displacement and deformation of the speckle pattern are then analyzed to determine the corresponding strain in the material.

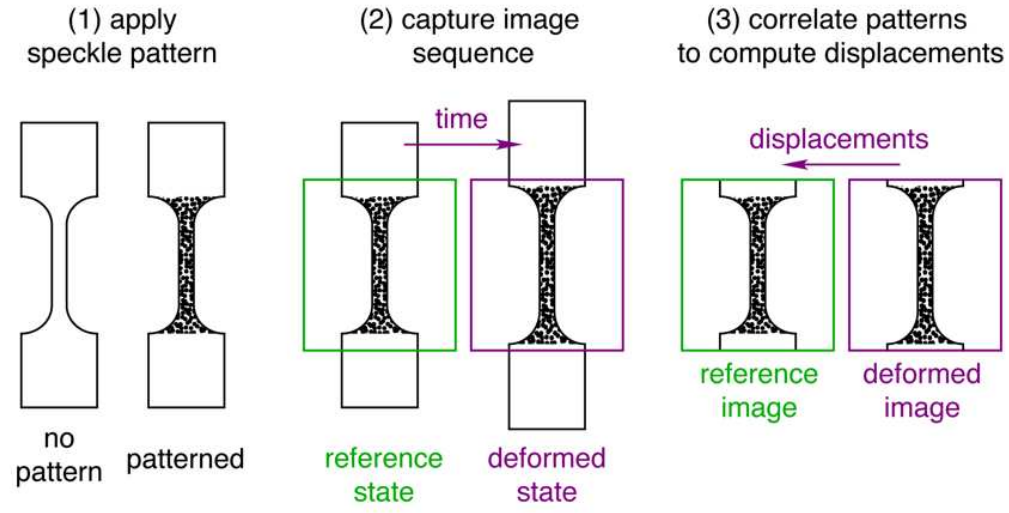

Figure 2.8: Process of a DIC experiment

2.3 Compression test

A compression test is a type of mechanical test used to determine the behavior of a material under compressive loading. It involves applying a compressive force to a specimen and measuring its response to deformation. The test helps characterize the material's compressive strength, deformation characteristics, and ability to withstand axial loads.
The examination specimen is compressed between two plates causing a compressive stress state. The test specimen dimensions, and geometry are provided from the norm ASTM D695-15, which suggests having a length twice the diameter. In this case, the specimens have a length of $20 \pm 1mm$ and a diameter of $10 \pm 1mm$. This test aims to get the curve stress-strain which describes the material's behavior under compressive load.

Definitions

Compressive Strength (σ_c): This is the maximum stress the material can withstand under compression. It is calculated by dividing the maximum load by the original cross-sectional area of the specimen.

$$\sigma_C = \frac{P}{A_0}[MPa]$$

where:

- σ_c is the compressive strength
- P is the maximum load applied during the test
- A_0 is the original cross-sectional area of the specimen

Compressive Modulus (Young's Modulus in Compression): Similar to Young's Modulus in tension, the compressive modulus reflects the material's stiffness under compressive loads. It is calculated as the slope of the initial linear portion of the stress-strain curve.

$$E_{compression} = \frac{\Delta\sigma}{\Delta\varepsilon}[MPa]$$

Strain at Failure (ε_f): The strain at failure represents the amount of deformation the material undergoes before failure. It is determined by measuring the strain at the point where the stress-strain curve reaches its maximum.

2.4 Tensile test setup and methodology

Equipment Setup: To conduct the tensile test, the INSTRON 3366 machine with a maximum capacity of 10kN was employed, making it well-suited for testing polymer specimens. It is crucial to synchronize data recording between the INSTRON machine and the Digital Image Correlation (DIC) camera. The acquisition timing for both instruments was carefully adjusted to ensure simultaneous data collection. A recording interval of two-tenths of a second was chosen to capture a sufficient number of data points for accurate analysis. Note that due to technical constraints, the DIC camera had to be initiated manually, potentially resulting in minimal misalignment between the two devices.

Test Parameters: The tensile test was executed at a strain rate of 1.5% per minute. Given the length of the dog-bone specimens (60 mm) between the clamping areas, the testing speed was set to 0.5 mm/minute. This speed, although lower than ASTM standards, was intentionally chosen to enhance data resolution and provide better control throughout the test.

Two-Step Testing Approach: The test protocol comprised two distinct steps to extract comprehensive data:

1. Loading and Unloading Phase: The first step involved subjecting the specimen to a loading phase until a strain of 0.25% was reached. Subsequently, an unloading phase was executed to return the specimen to its original elongation. This phase aimed to capture crucial mechanical properties, namely the Elastic Modulus and the Poisson ratio, within the linear elastic region of the material.

2. Failure Testing: The second step involved loading the specimen until it fractured. This phase aimed to obtain key mechanical parameters such as Tensile Strength and Strain to Failure. The choice to conduct the test until failure provides a comprehensive understanding of the material's behavior under extreme conditions.

2.5 Compressive test and methodology

Similar to the tensile test, the compressive tests were conducted utilizing the INSTRON 3366 machine. While the DIC machine was not employed for this test cause the impossibility for it to read the change in position of the various dots. For this test to read the strain it has been used the sensor from the INSTRON machine.

Test Parameters**:** The compressive tests were conducted at a strain rate of 5% per minute. Considering the cylindrical specimen's length of 20±1 mm between the two ends, the testing speed was set to 0.1 mm/minute.

Testing Approach*:* The compressive test involved loading the specimen until failure occurred under compression. This approach aimed to extract crucial mechanical

parameters, specifically Compressive Strength and Compressive Strain to Failure. Unlike tensile testing, compressive testing investigates the material's ability to withstand forces acting to shorten or compress it, providing valuable insights into its structural integrity and behavior under compression.

2.6 SEM

To compare and verify the microstructure of the SBE used in the tests i.e. obtained by a polymer deposition on a surface and the reference microstructure obtained by vacuum infusion presented in the previous published work a SEM has been performed.
Scanning electron microscopy (SEM) is a powerful tool used to visualize the intricate details of objects at a microscopic level, reaching down to the nanoscale. This remarkable technology employs a focused beam of electrons to bombard the surface of a sample, inducing interactions that generate various signals. These signals, captured by specialized detectors, are then processed, and interpreted to create a detailed image of the sample's morphology and composition.
At the heart of an SEM lies the electron gun, which is the source of this energetic beam. A heated filament emits electrons, which are then accelerated through a high-voltage field, gaining immense kinetic energy. These electrons then enter a series of electromagnetic lenses that further focus and refine the beam, ensuring precise sample illumination.
A sophisticated computer system amplifies, digitizes, and processes the captured signals from the detectors. The computer assigns different intensities or colors to the signals, creating a detailed image that reflects the sample's surface morphology and composition. The resulting SEM images are often highly magnified, revealing intricate details invisible to the naked eye or even conventional optical microscopes.

2.6.1 Specimen preparation

To observe the porous microstructure the polymer must be dried from its liquid phase and then a spatter coating applied.

- Drying phase: In this phase, the polymer is dried through 2 main simple steps. The first consists of keeping the SBE in water for 3 days and changing the water every 12 hours to ensure the liquid from the inside moved out through a concentration gradient. The second step consists of drying the polymer in the oven for 48 hours to ensure that all the liquid particles evaporate resulting in a perfectly dried specimen.

- Spattering phase: Spatter coating is the process of depositing a thin conductive film on a non-conductive sample surface to prevent the build-up of static charge during scanning electron microscopy (SEM). The static charge can cause the image to appear distorted or blurry. There are several ways to spatter coat a sample, but the most common method is to use a sputter coater. A sputter coater is a vacuum chamber that contains a target made of the desired conductive material. A gas, typically argon, is introduced into the chamber and ionized by an

electric field. The ionized gas atoms collide with the target, knocking off atoms that are then deposited onto the sample surface.

2.7 Shrinkage test

To assess whether the material experiences shrinkage during the curing process, a shrinkage test is conducted. This evaluation is crucial as it helps determine if any changes in volume occur during curing. Additionally, it aids in assessing whether the material may undergo prestressing within the Structural Battery. Understanding these aspects is fundamental for ensuring the structural integrity and performance of the material in the given application. Shrinkage is a common phenomenon observed in polymers during the curing process, especially in thermosetting polymers. The curing process involves the transformation of a polymer from a liquid or soft state to a hardened or solid state. This transformation is often accompanied by changes in volume, which can result in shrinkage. The shrinkage effects during the curing process in polymers can be attributed to several factors:

Chemical Reactions:

- Crosslinking: In many polymer systems, curing involves the formation of crosslinks between polymer chains. The creation of these crosslinks can lead to a reduction in the overall free volume of the polymer, resulting in shrinkage.
- Polymerization: Monomers polymerize to form larger polymer chains during the curing process. The conversion of small molecules into larger, more closely packed polymer chains can contribute to volumetric shrinkage.

  Loss of Volatile Components:
- Some polymer systems involve the evaporation or removal of volatile components during curing. The loss of these components can lead to a decrease in volume.

  Physical Changes:
- Crystallization: In certain polymers, curing can induce crystallization, which often results in a reduction in volume due to the more ordered and closely packed molecular structure.

  Contraction During Cooling:
- As the cured polymer cools down from the elevated temperature of the curing process, it may undergo additional contraction, contributing to the overall shrinkage.

Test Preparation:

Similar to the procedure used for preparing specimens for the compression test, the process for this case followed a consistent routine. It involved depositing the polymer into syringes and allowing it to cure. However, in this instance, the syringes were marked before the curing process. This modification was implemented to assess any potential changes in volume that might occur after the curing process.

THEORY

3.1 Constitutive behavior of materials

In this section, the constitutive theory regarding elasticity, hyperelasticity, and the Von Mises yield criteria are discussed.

3.1.1 Elasticity

In the realm of material mechanics, various materials exhibit a spectrum of elastic behaviors. A linear elastic behavior is characterized by a precise proportionality between applied load (F) and resulting displacement (Δ) at each loading and unloading stage. This linear relationship is governed by the spring constant (k). It's worth noting that many solid materials possess a range within which their behavior adheres to the principles of linear elasticity, making them amenable to description through Hooke's law, as expressed in equation 3.1. A visual representation of this linear relationship is provided in Figure 3.1.

$$F = k\Delta \quad (3.1)$$

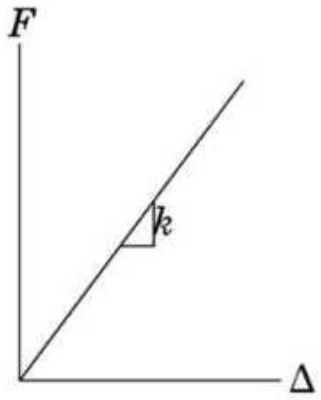

Figure3.1: Hooke’s law

The mechanical strength of a material is quantified through stress, denoted as σ. In the context of uniaxial tension, this relationship follows Hooke's law, where the spring constant (k) is substituted by Young's modulus (E), and the displacement (Δ) is replaced with strain (ε). This relationship is mathematically described in equation 3.2.

$$\sigma = E\varepsilon \quad (3.2)$$

3.1.2 Hyperelasticity

A material displaying hyperelastic behavior does not conform to the straightforward Hookean spring-like response, where stress and strain exhibit a linear relationship. Instead, hyperelastic materials exhibit a nonlinearity in the stress-strain relationship, relying solely on the initial and final states of deformation. The establishment of hyperelastic models, particularly for isotropic materials, is grounded in the concept of strain energy potential. In this framework, it is postulated that a strain energy density function (Ψ) exists, and its dependence is on either the strain or deformation tensors. Strain energy density is a measure of the internal elastic energy stored within a material due to deformation or strain. It represents the potential energy stored in the material as a result of the change in shape or deformation. Equation 3.3 within this context provides the expressions for the components of the second Piola-Kirchhoff stress tensor, (S_{ij}). This tensor is a fundamental element in characterizing the stress in hyperelastic materials and serves as a key component in understanding their complex mechanical behavior.

$$S_{ij} = \frac{d\Psi}{dE_{ij}} = 2\frac{d\Psi}{dC_{ij}} \quad (3.3)$$

The Langrangian strain tensor components are defined as (E_{ij}) and can be expressed as in equation 3.4. The Cauchy-Green deformation tensor is defined as the components (Cij) which are expressed as in equation 3.5.

$$E_{ij} = \frac{1}{2}(C_{il} - \delta_{ij}) \quad (3.4)$$

Where δ represents the identity matrix, where $\delta_{ij} = 1$ when $i = j$ and $\delta_{ij} = 1$ when $i \neq j$.

$$C_{ij} = F_{ki}F_{kj} = \frac{dx_k}{dx_i}\frac{dx_k}{dx_j} \quad (3.5)$$

Where the components of the second Piola-Kirchhoff stress tensor are defined as (Fij). In this context, (X_i) represents the initial position of a point along the direction (i), while (x_i) denotes the deformed position of the same point along the direction (i). The displacement of the point in a direction (i) is represented as (u_i), and it defines the change from the initial to the deformed position: $x_i = X_i + u_i$. We introduce the principal stretch ratios, denoted as λ_1^2, λ_2^2, and λ_3^2 which are determined by the eigenvalues of the tensor C_{ij}. It's important to note that these principal stretch ratios exist only when equation 3.6 is satisfied.

$$\det\left[C_{ij} - \lambda_p^2\delta_{ij}\right] = 0 \Longrightarrow \lambda_p^6 - I_1\lambda_p^4 + I_2\lambda_p^2 - I_3 = 0 \quad (3.6)$$

The invariants of C_{ij} are I_1, I_2, and I_3 are defined in equation 3.7.

$$I_1 = tr(C) = \lambda_1^2 + \lambda_2^2 + \lambda_3^2 \quad (3.7.a)$$
$$I_2 = \lambda_1^2\lambda_2^2 + \lambda_2^2\lambda_3^2 + \lambda_1^2\lambda_3^2 \quad (3.7.b)$$
$$I_3 = \lambda_1^2\lambda_2^2\lambda_3^2 = J^2 = \det(C_{ij}) \quad (3.7.c)$$

Where $J = \det(F_{ij})$ and it represents the ratio of the deformed elastic volume to the original (unchanged) volume. It quantifies the volumetric change or deformation experienced by a material under the application of external loads or forces. The strain energy function in a general form can be expressed as the polynomial 3.8.

$$\Psi = \sum_{i+j=1}^{N} C_{ij}(I_1 - 3)^i (I_2 - 3)^j + \sum_{i=1}^{N} \frac{1}{D_i}(J-1)^{2i} \quad (3.8)$$

Where (D_i) is a material constant related to the shear modulus and the bulk modulus.

$$D_i = \frac{\lambda_L}{2} \quad (3.9)$$

Where (λ_L) equation 3.10, corresponds to the first Lamé parameter which is a measure of a material resistance to change in volume; is related to the material's bulk modulus and shear modulus.

$$\lambda = \frac{E\nu}{(1+\nu)(1-2\nu)} = K - \frac{2}{3}\mu \quad (3.10)$$

Where (K) and (μ) correspond to the bulk modulus and shear modulus respectively. The assumption of the material being incompressible gives that $J=1$ leading to the following strain energy function 3.11.

$$\Psi = \sum_{i+j=1}^{N} C_{ij}(I_1 - 3)^i (I_2 - 3)^j \quad (3.11)$$

3.1.3 Ogden model

The strain energy function according to Ogden's definition is a function of the principal stretch ratios from the left Cauchy strain tensors 3.12.

$$\Psi = \sum_{i=1}^{N} \frac{\mu_i}{\alpha_i}\left(\lambda_1^{\alpha_i} + \lambda_2^{\alpha_i} + \lambda_3^{\alpha_i} - 3\right) + \sum_{i=1}^{N} \frac{1}{D_i}(J-1)^{2i} \quad (3.12)$$

Where N is the number of terms, (α_i) and (μ_i) are material constants and are determined experimentally. Again, assuming incompressible material (i.e., $J=0$) equation 3.12 is reduced to the expression in equation 3.13.

$$\Psi = \sum_{i=1}^{N} \frac{\mu_i}{\alpha_i}\left(\lambda_1^{\alpha_i} + \lambda_2^{\alpha_i} + \lambda_3^{\alpha_i} - 3\right) \quad (3.13)$$

3.1.4 Isotropic plasticity

The stress of a material can be defined by its nine components as expressed in equation 3.14.

$$\sigma_{ij} = \begin{bmatrix} \sigma_{xx} & \sigma_{xy} & \sigma_{xz} \\ \sigma_{yx} & \sigma_{yy} & \sigma_{yz} \\ \sigma_{zx} & \sigma_{zy} & \sigma_{zz} \end{bmatrix} = \begin{bmatrix} \sigma_{11} & \sigma_{12} & \sigma_{13} \\ \sigma_{21} & \sigma_{22} & \sigma_{23} \\ \sigma_{31} & \sigma_{32} & \sigma_{33} \end{bmatrix} \quad (3.14)$$

The region surrounding the stress space's origin is designated as the elastic zone. The periphery of this region is referred to as the initial yield surface, which can be mathematically described by equation 3.15. In a three-dimensional stress space, this surface takes on a cylindrical shape, as illustrated in Figure 3.2.

$$f(\sigma_{ij}) = constant \quad (3.15)$$

Assuming isotropic material properties, plastic yielding is independent of the directions of the principal stresses but solely on their magnitude. This leads to that the yield is a symmetric function of the principal stresses ($\sigma_{ij} = \sigma_{ji}$), making it solely dependent on the principal components of the deviatoric stress tensor (s_{ij}) defined in equation 3.16.

$$s_{ij} = \sigma_{ij} - \sigma_{HYD}\delta_{ij} \quad (3.16)$$

Where (σ_{HYD}) represents the hydrostatic stress defined as the trace of the (σ) matrix divided for 3, it is a scalar representing the average normal stresses on the faces of an infinitesimal cube, defined in equation 2.37. The hydrostatic stress tensor is responsible for changing the volume of the body and the deviatoric stress tensor is responsible for changing the shape of the material while keeping the volume constant. An illustration of this decomposition is shown in Figure 3.3.

$$\sigma_{HYD} = \frac{tr(\sigma)}{3} = \frac{\sigma_{11}+\sigma_{22}+\sigma_{33}}{3} \quad (3.17)$$

3.1.5 Von Mises yield criteria

According to the Von Mises yield criterion, yielding takes place when the Von Mises stress (σ_{VM}) function of the second invariant of the deviatoric stress tensor reaches the yield stress (σ_Y) in uniaxial tension. Those are expressed in equations 3.18 and 3.19 respectively.

$$\sigma_{VM} = \sqrt{-3I_2(S)} = \sqrt{\frac{3}{2}I_1(SS)} = \sqrt{\frac{3}{2}\sum_{i,j=1}^{3} S_{ij}S_{ij}} = \sqrt{3J_2} \quad (3.18)$$

$$J_2 = \sqrt{\frac{1}{2}[(\sigma_{11}-\sigma_{22})^2 + (\sigma_{22}-\sigma_{33})^2 + (\sigma_{11}-\sigma_{33})^2 + 2({\sigma_{12}}^2 + {\sigma_{13}}^2 + {\sigma_{23}}^2)]} \quad (3.19)$$

Where (J_2) represents the second invariant of the deviatoric stress.

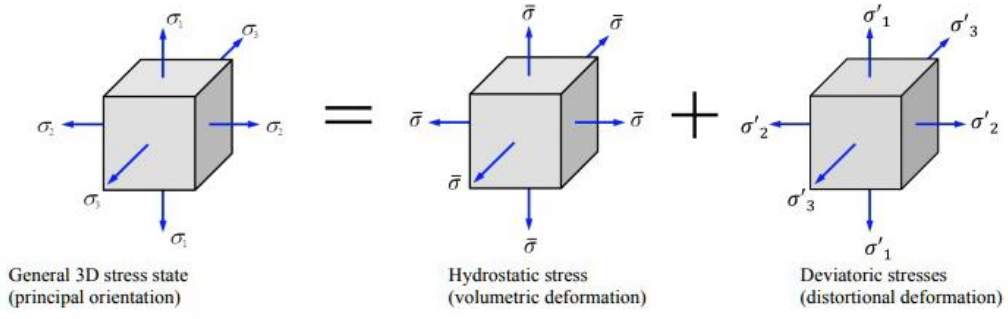

Figure 3.3: Decomposition of a 3D stress element

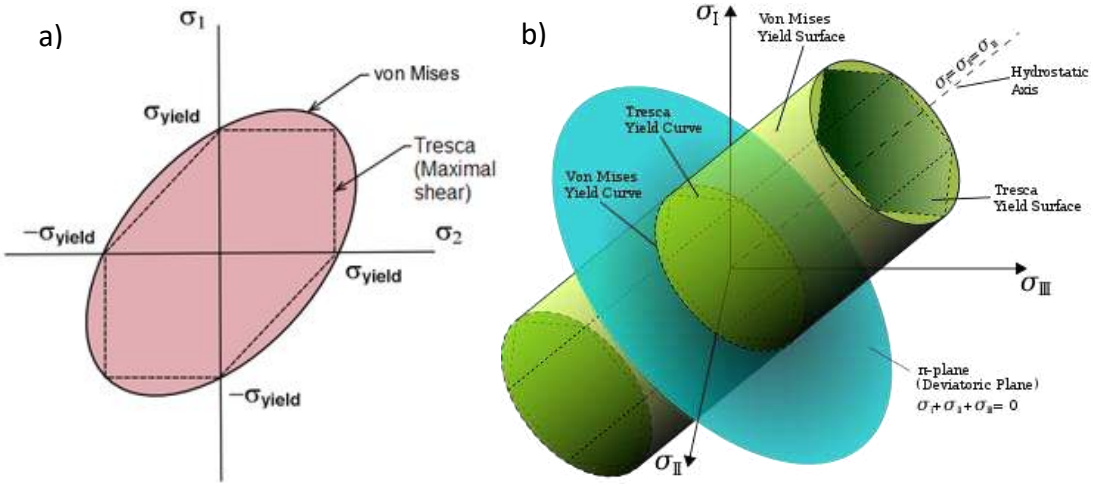

Figure 3.2: a) Representation of the Von Mises Yield surface in two-dimensional space, b) 3D representation of Von Mises Yield surface.

3.2 Raghava yield criteria

The Von-Mises yield criterion does not predict differences in yield stress between compression and tension. Modifications of the Von-Mises criterion have incorporated the effect of hydrostatic stress into equation 3.20. The modified Von-Mises criterion can in general form be written as

$$A(\sigma_1 + \sigma_2 + \sigma_3) + B[(\sigma_1 - \sigma_2)^2 + (\sigma_2 - \sigma_3)^2 + (\sigma_3 - \sigma_1)^2] = 1 \quad (3.20)$$

It is possible to define the constants A and B in terms of the simple uniaxial compressive and tensile yield stresses, (σ_{yc}) and (σ_{yt}) respectively. This will give the yield criterion suggested by Raghava et al [29].

$$2(\sigma_{yc} - \sigma_{yt})(\sigma_1 + \sigma_2 + \sigma_3) + [(\sigma_1 - \sigma_2)^2 + (\sigma_2 - \sigma_3)^2 + (\sigma_3 - \sigma_1)^2] = 2\sigma_{yc}\sigma_{yt} \quad (3.21)$$

3.3 FEM model

After acquiring the mechanical values, it is crucial to elucidate the material's behavior within the Structural Battery. The lithiation and delithiation phases play an important role in the polymer's performance, as the swelling of the carbon fiber poses a potential risk. In the lithiation phase, the carbon fiber within the negative electrode accepts lithium atoms, leading to pronounced swelling with a large radial expansion of 6.6 % and an axial expansion of 0.85 % of the fibers. This swelling is particularly notable along the radius, where the most significant changes can be observed. Similarly, the delithiation process mirrors this phenomenon, wherein lithium from the fibers within the negative electrode migrates toward the positive electrode. During this stage, the fibers release lithium and revert to their original form concurrently. The lithiation process induces elevated stresses within the matrix due to the expansion of fibers, leading to highly stressed regions, especially in the space between two fibers where significant compression zones occur. These highly stressful processes for the material are observed through a 3D Finite Element Model (FEM), which simulates its behavior. This allows us to check if the material undergoes failure. The model in reference is made by Carl Larsson [30], which takes into consideration the effects of lithium insertion-induced swelling of a structural battery negative electrode.

3.3.1 Preliminaries

The microscale analysis is performed on a synthetical, assumed representative volume element (RVE). The RVE domain,$\Omega_{X,\blacksquare}$ indicated by the box ■, consists of the carbon fiber domain, $\Omega_{X,\blacksquare}^{cf}$, and the SBE domain, $\Omega_{X,\blacksquare}^{SBE}$, with $\Omega_{X,\blacksquare} = \Omega_{X,\blacksquare}^{cf} \cup \Omega_{X,\blacksquare}^{SBE}$, as illustrated in Figure 3.3.

To analyze the effects of lithiation/delithiation of the carbon fibers on the performance of a structural battery, knowledge about the charge cycle and rate is needed. The state of lithiation is defined as

$$c(t) = \frac{c_{Li}(t)}{c_{Li}^{max}} \quad (3.22)$$

Where $c_{Li}(t)$ is the concentration of lithium, and c_{Li}^{max} denotes the reference maximum concentration of lithium, for a certain charge rate. This equation is applicable for conditioned fibers, i.e., when studying fibers with a reversible capacity in the structural electrode. For unconditioned fibers, the varying maximum lithium concentration with respect to the charge cycle must be considered. The state of lithiation for charge cycle i, $(c(t))_i$, is expressed as

$$(c(t))_i = \frac{c_{Li}(t)}{(c_{Li}^{max})_i} \quad (3.23)$$

Where $(c_{Li}^{max})_i$ represents the reference maximum concentration that can be inserted into the electrode during the ith lithium insertion/desertion cycle.

Is considered an extreme scenario by assuming a uniform distribution of c within $\Omega_{X,\blacksquare}^{cf}$.

Throughout electrochemical cycling, the carbon fibers (X) undergo expansion and contraction due to the insertion and removal of lithium. These changes in volume induce internal stresses within the composite material.

The internal stresses resulting from lithiation are influenced by the external boundary conditions acting on the composite.

If the composite material is subjected to external constraints preventing its expansion, as depicted in Figure 3.2 b, it is anticipated that internal stresses of high magnitude will develop. On the contrary, if the composite is unconstrained, allowing for unrestricted expansion, as shown in Figure 3.2 c, lower magnitudes of internal stresses are expected.

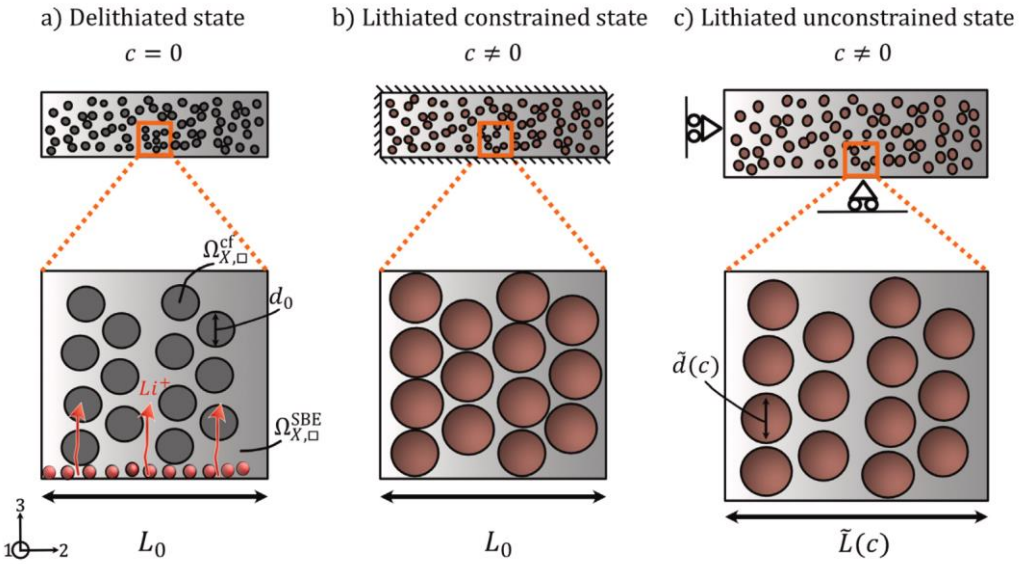

Figure 3.3: Two-dimensional illustration of morphology change as carbon fibers are lithiated. a) Delithiated RVE with initial side length L_0 and carbon fiber diameter d_0, b) Lithiated, fully constrained, RVE such that the side length remains at L_0, c) Lithiated, unconstrained RVE, whereby the side length increases, $L(c) > L_0$ [29].

3.3.2. Constitutive model for the fiber domain, $\Omega_{\blacksquare}^{cf}$

Consider a fiber that swells due to lithium insertion with uniform concentration c. In the finite deformation setting, is adopted a multiplicative decomposition of the deformation gradient as

$$F = \bar{F} \cdot F^{ch}(c) \quad (3.24)$$

Where $F^{ch}(c)$ contributes to a chemical expansion, and $\bar{F}$ represents an elastic deformation as shown in Figure 3.4.

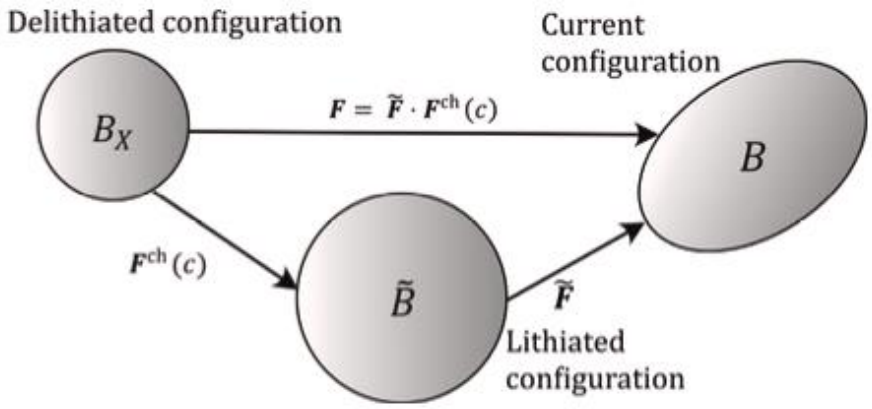

Figure 3.4: Multiplicative split of the deformation gradient in the carbon fiber. Starting from the delithiated (reference) configuration B_X, the domain is expanded to $\bar{B}$ after lithiation (function of c), finally deformed elastically to B [29].

To model elasticity for stress free deformation, we express the volume-specific free energy for a given state of lithiation c as

$$\psi_X(c,F) = J^{ch}\tilde{\psi}\left(c,\tilde{F}\right) \quad (3.25)$$

Where $J^{ch} = det\left(F^{ch}(c)\right)$ and $\tilde{\psi}$ is the free energy per unit volume in the lithiated configuration $\tilde{B}$. The first Piola-Kirchhoff stress tensor becomes

$$\tilde{P} = \frac{\partial\tilde{\psi}}{\partial\tilde{F}} = \frac{1}{J^{ch}(c)} P \cdot [F^{ch}(c)]^T \quad (3.26)$$

Considering the Green Lagrange strain tensor $\tilde{E}(c)$ represents the apparent linear elasticity tangent stiffness for a stress-free, lithiated carbon fiber. In the lithiated configuration $\tilde{B}$, it is expressed the intermediate first Piola-Kirchhoff stress using the Saint-Venant model from the lithiated configuration $\tilde{B}$ as

$$\tilde{P} = \tilde{F} \cdot \tilde{S} \text{ with } \tilde{S}\left(c,\tilde{E}\right) = \tilde{E}(c) : \tilde{E} \quad (3.27)$$

Where

$$\widetilde{E} := \frac{1}{2}\left[\tilde{C} - I\right], \tilde{C} = \tilde{F}^T \cdot \tilde{F} = [F^{ch}]^{-T} \cdot C \cdot [F^{ch}]^{-1} \quad (3.28)$$

With $\tilde{S}$ that represents the intermediate second Piola-Kirchhoff stress tensor. Using expressions (3.26) and (3.28) is possible to express the first Piola-Kirchhoff stress as

$$P(c,F) = J^{ch}(c)\tilde{P}(c,F) \cdot [F^{ch}(c)]^{-T} \quad (3.29)$$

This is the complete model parametrized in the concentration c.

3.3.3 Constitutive model for the structural battery electrolyte domain, $\Omega_{\blacksquare}^{SBE}$

The material model is supposed to be isotropic hyperelastic neo-Hookean for the SBE matrix, whereby the second Piola-Kirchhoff stress $S(C)$ is decomposed into volumetric and isochoric parts. The volumetric part represents the stress contribution associated with changes in volume due to hydrostatic pressure while the isochoric part represents a deformation that preserves the local volume at every point. At this point, we can write

$$P(F) = F \cdot S(C) \quad (3.30)$$

$$S(C) = KJ[J-1]C^{-1} + GJ^{-2/3}\left[I - \frac{1}{3}(C:I)C^{-1}\right] \quad (3.31)$$

Where $J = det(F) = \sqrt{det(C)}$, K is the bulk modulus, and G is the shear modulus of the SBE. Given the available measurements of linear elastic isotropic material parameters, it has been opted for the neo-Hookean model that effectively addresses significant volumetric deformations. The mechanical characteristics of the SBE are detailed in Table 2. It is acknowledged that the neo-Hookean model may not offer precise predictions, especially under substantial compression. However, in the absence of more comprehensive measurement data, is regards the neo-Hookean model is a viable extension of linear elasticity, providing a reasonable approximation until more detailed experimental information becomes available.

Table 2. Mechanical properties for carbon fibers and SBE [28].

Carbon fibers	Source
$E_L = 294\ GPa$	[31]
$E_T = 21.8\ GPa$	[31]
$v_{TT} = 0.2$	Assumed
$v_{LT} = 0.22$	Assumed
$\alpha_T = 0.066$	[31]
$\alpha_L = 0.0085$	[32]
$G_{LT} = 12.5\ GPa$	Assumed
SBE	
$E = 0.7\ GPa$	[25]
$v = 0.37$	Assumed

RESULTS AND DISCUSSION

4.1 Tensile test results

After completing a comprehensive series of tests on seven specimens, to make the results from the tests reliable, a thorough post-processing phase was conducted to analyze the acquired data, enabling precise considerations.

Elastic Modulus and Poisson Ratio Results:
Table 3. below presents the results for the Elastic Modulus and Poisson Ratio obtained during the unloading phase from 0.25% strain, back to the original position for each specimen:

Table 3. Tensile test, Elastic modulus, and Poisson's ratio until 0.25% in strain.

Specimen	Elastic Modulus (MPa)	Poisson Ratio
1	420.43	0.33
2	406.40	0.29
3	447.18	0.29
4	593.02	0.57
5	509.72	0.40
6	327.25	0.33
7	363.82	0.37

Considerations:

- Specimen 4: Elastic Modulus and Poisson Ratio results from the first test are not considered due to potential misalignment, resulting in values outside the expected range.

Tensile Strength and Tensile Strain to Failure Results:
Table 4. summarizes the results for Stress to Failure and Strain to Failure obtained during the second test, conducted until specimen failure:

Table 4. Tensile test, Tensile strength, and Strain to failure

Specimen	Tensile Strength (MPa)	Strain to Failure (%)
1	4.612	2.14
2	Not applicable (premature failure)	Not applicable
3	4.68	2.27
4	4.63	2.28
5	3.89	Not applicable
6	5.23	2.62
7	6.034	3.15

Considerations:

- Specimen 2: Premature failure occurred during the extension due to a sample defect, leading to an earlier breaking.
- Specimen 5: Strain data is not included in the analysis due to technical issues encountered by the DIC during recording.

These findings encapsulate the material's response to tensile loading along a uniaxial direction. The subsequent Table 5. presents the average values for each parameter type.

Table 5. Tensile test outcomes

	Elastic Modulus (MPa)	Poisson's Ratio	Tensile Strength (MPa)	Strain to Failure (%)
AVERAGE VALUE	412.47	0.34	4.85	2.49

Final Considerations:

The material generally demonstrates a highly brittle behavior, characterized by a minimal strain capacity before failure. The initial elastic linear region reveals a limited deformation capability, and beyond this phase, the material exhibits a pronounced non-linear behavior as shown in Figure 4.3. This brittleness is indicative of a rapid and abrupt failure mode, showcasing the material's sensitivity to applied tensile stress as shown in Figures 4.4 and 4.5 where it is possible to see the breaking fracture of specimens n.1 and n.3.

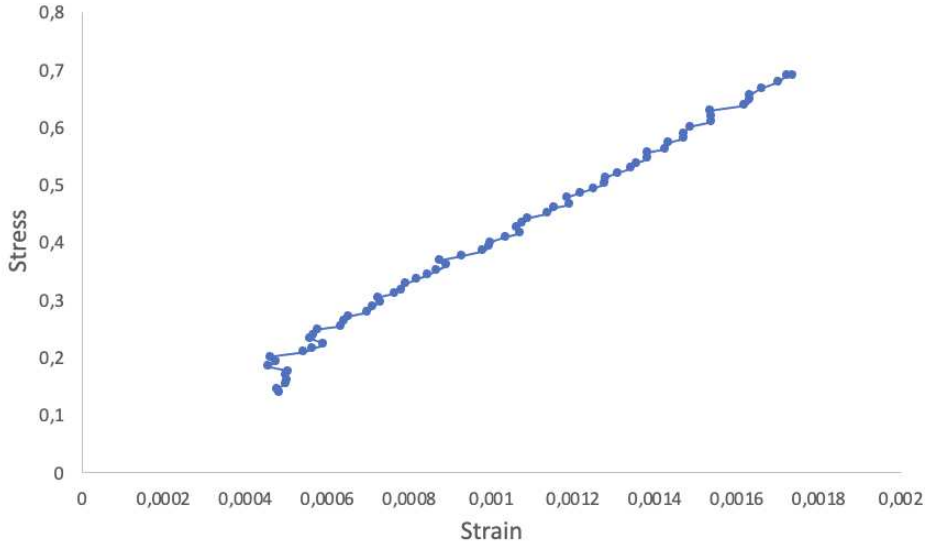

Figure 4.1: Stress-strain curve in the linear-elastic region.

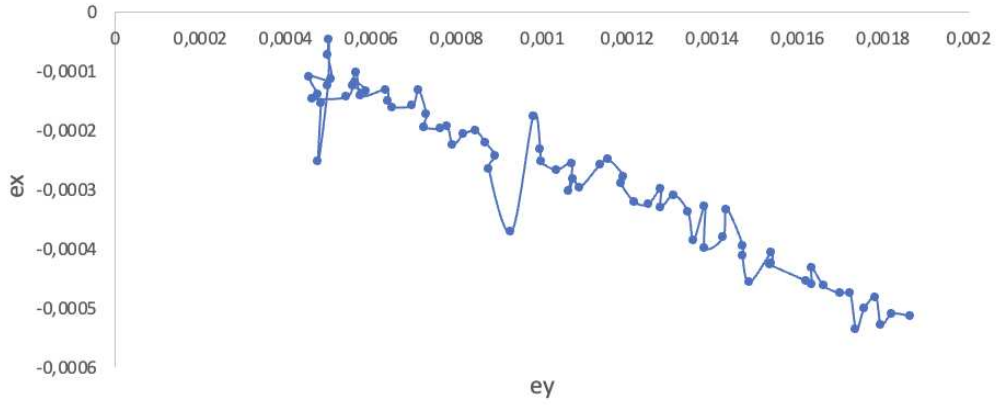

Figure 4.2: Strain curve in longitudinal and transverse directions in the elastic region.

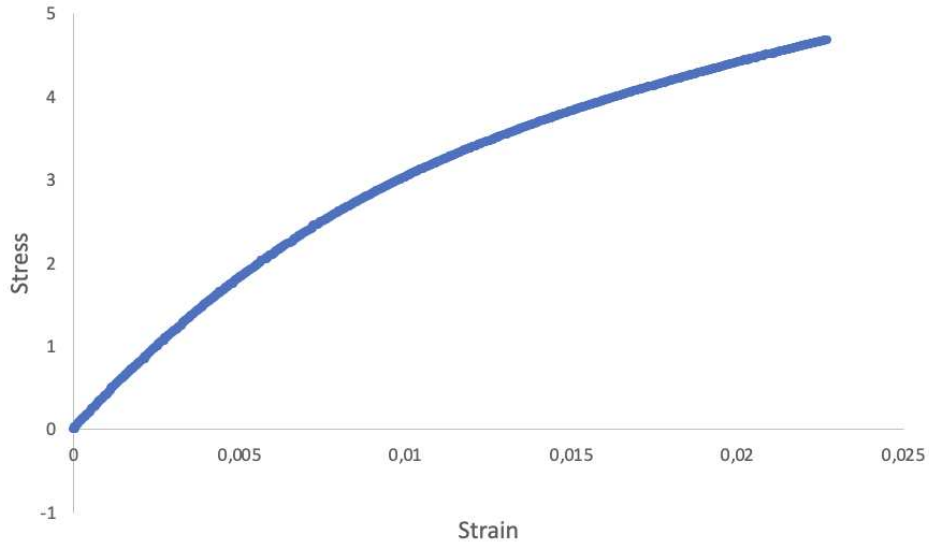

Figure 4.3: Stress-strain curve until failure.

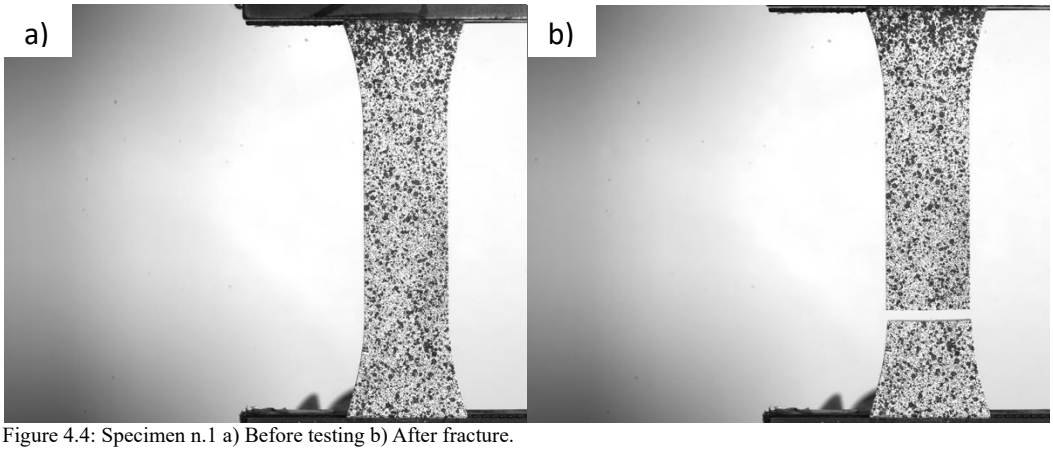

Figure 4.4: Specimen n.1 a) Before testing b) After fracture.

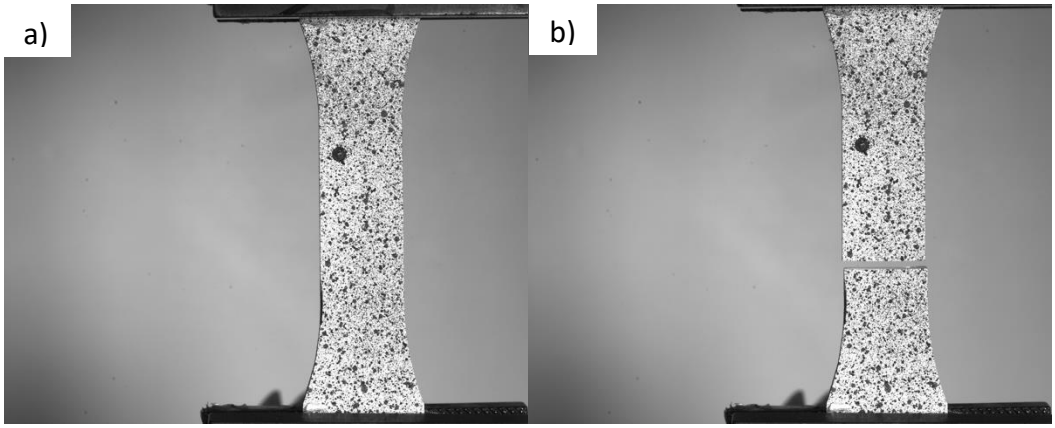

Figure 4.5: Specimen n.3 a) Before testing b) After fracture.

4.2. Compression test results

While the DIC machine was not employed for the main testing, one preliminary test involved a speckled surface to capture images before and after failure, Figure 4.6.
Another attempt used three aligned dots marked with a Sharpie to simulate a flat surface for DIC observation. Unfortunately, this effort proved unsuccessful as the liquid electrolyte seeped from the pores, rendering the marked points illegible for DIC analysis, Figure 4.7.
After completing a comprehensive series of tests on six specimens, to make the results from the tests reliable, a thorough post-processing phase was conducted to analyze the acquired data, enabling precise considerations.

Compressive Strength and Compressive Strain to Failure Results:

Table 6. summarizes the results for Compressive Strength and Compressive Strain to Failure obtained during the test, conducted until specimen failure:

Table 6. Compression tests, Compressive Strength, and Compressive Strain to Failure

Specimen	Compressive Strength (MPa)	Strain to Failure (%)
1	31.66	30.70
2	32.97	28.26
3	31.59	27.13
4	33.52	28.81
5	32.62	27.89
6	32.61	28.45

Considerations:

In this case, the results appear very homogeneous, even though correlation with the DIC was not feasible. The consistent response to the compression load allows us to utilize these machine results without the need for correlation to the DIC.

These findings encapsulate the material's response to compressive loading along a uniaxial direction. The subsequent Table 7. presents the average values for each parameter type.

Table 7. Compression test outcomes

	COMPRESSIVE STRENGTH (MPa)	COMPRESSIVE STRAIN TO FAILURE (%)
AVERAGE	32.49	28.54

Final considerations:

The polymer consistently demonstrates a uniform behavior, characterized by a homogeneous barrel distortion with crack initiation originating from the center of the cylinder opening and propagating in the vertical direction, as illustrated in Figure 4.8.

In this case, as in the tensile test, the SBE exhibits a non-linear behavior, but this time it shows a way larger Strain to failure and larger Strength than the tensile test.
The reason for this difference between compression and tension is due to the nature of brittle materials:

- Brittle Fracture Mechanism*:* It fails through a mechanism called brittle fracture, where little or no plastic deformation occurs before failure. In compression, however, brittle materials exhibit a more gradual failure mode, allowing for higher Compressive strength and higher Strain to failure.

- Void Growth and Coalescence*:* Under tension, brittle polymers can be more susceptible to rapid crack propagation due to void growth and coalescence. In compression, the voids may not grow and coalesce as quickly, contributing to higher Compressive strength.

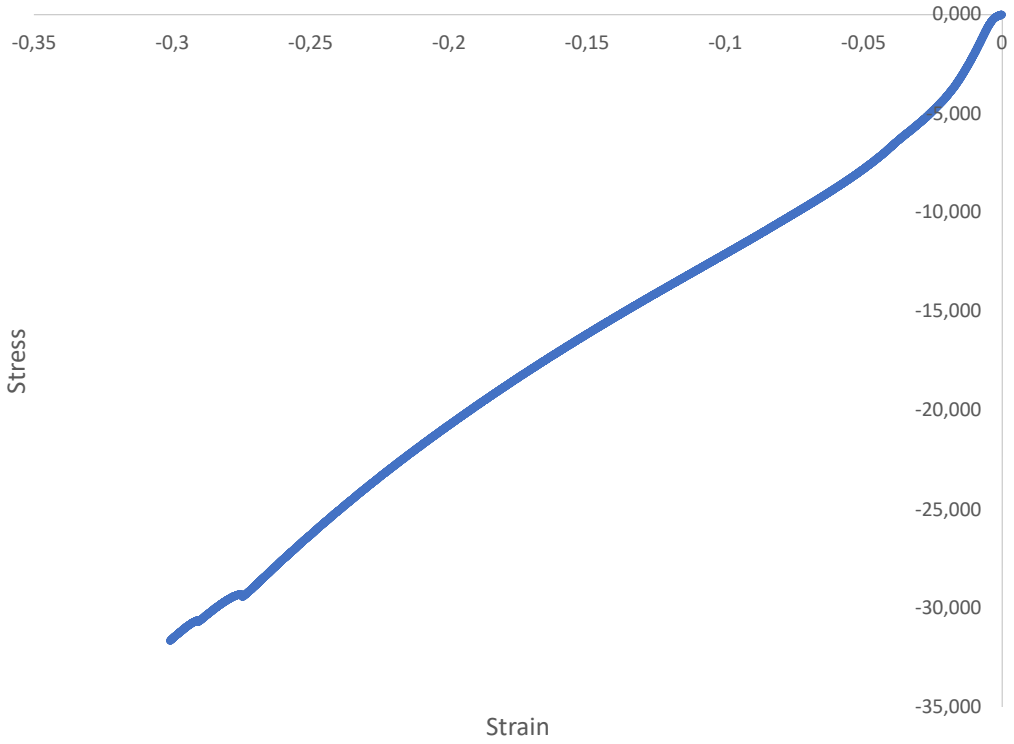

Figure 4.9: Stress-strain compression curve for specimen n.1.

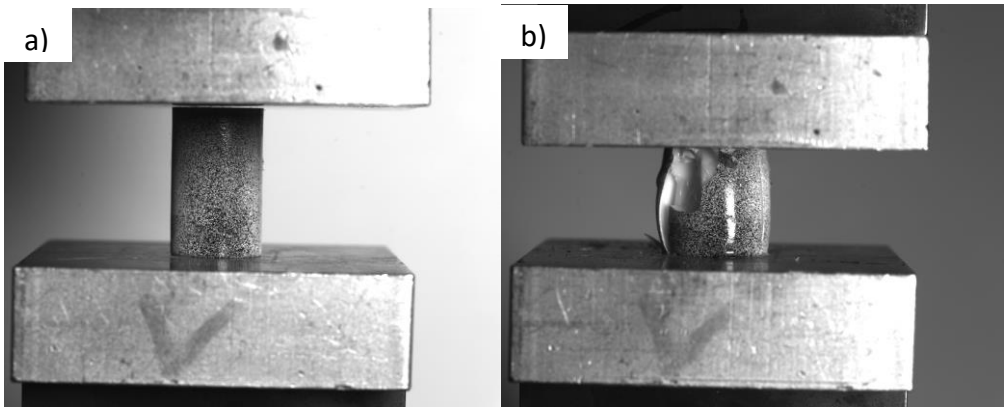

Figure 4.6: Speckled Cylinder specimen: a) Before testing, b) After breaking moment.

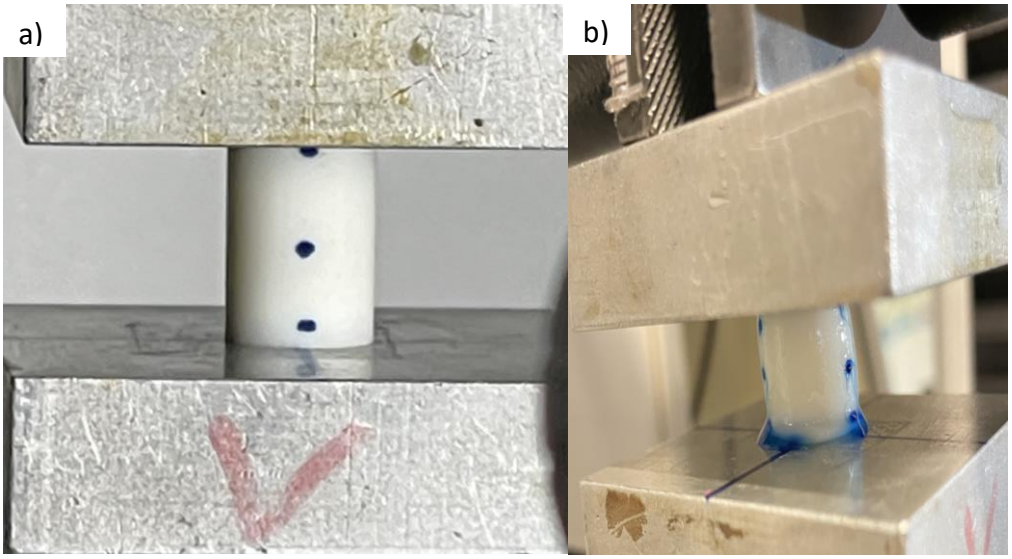

Figure 4.7: Dotted specimen: a) Before testing, b) Leaking of liquid electrolyte.

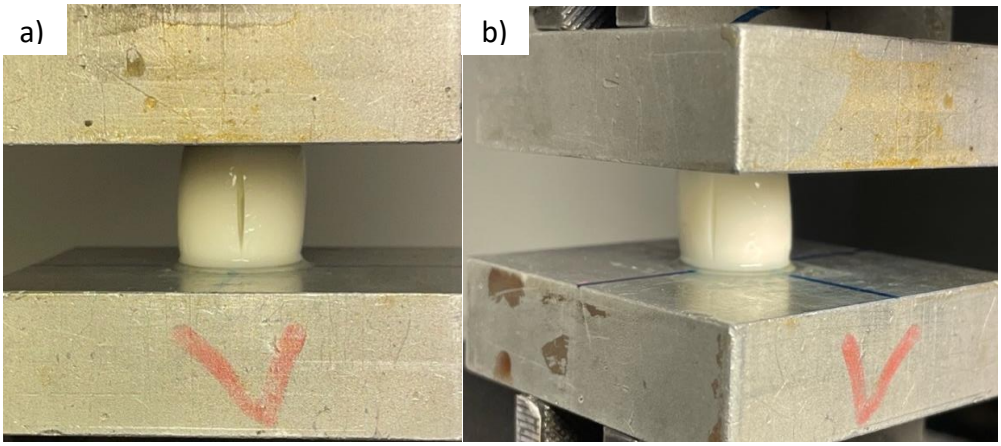

Figure 4.8: Barreling and crack propagation: a) From a frontal view, b) From a diagonal view.

4.3 Test considerations

To gain deeper insights into the mechanical characteristics of the SBE, a comprehensive graph with all the tests has been generated, illustrating both the tensile and compressive behaviors of the material under corresponding loads, as shown in Figure 4.9. The SBE exhibits a non-linear response, with tension showcasing a simpler behavior compared to compression. This distinction can be attributed to the heightened visibility of brittle behavior in tension, leading to sudden and premature failure. In contrast, compression reveals a less abrupt crack propagation, resulting in a more irregular behavior. Notably, the material demonstrates a significantly higher strength and strain at the point of rupture under compression.

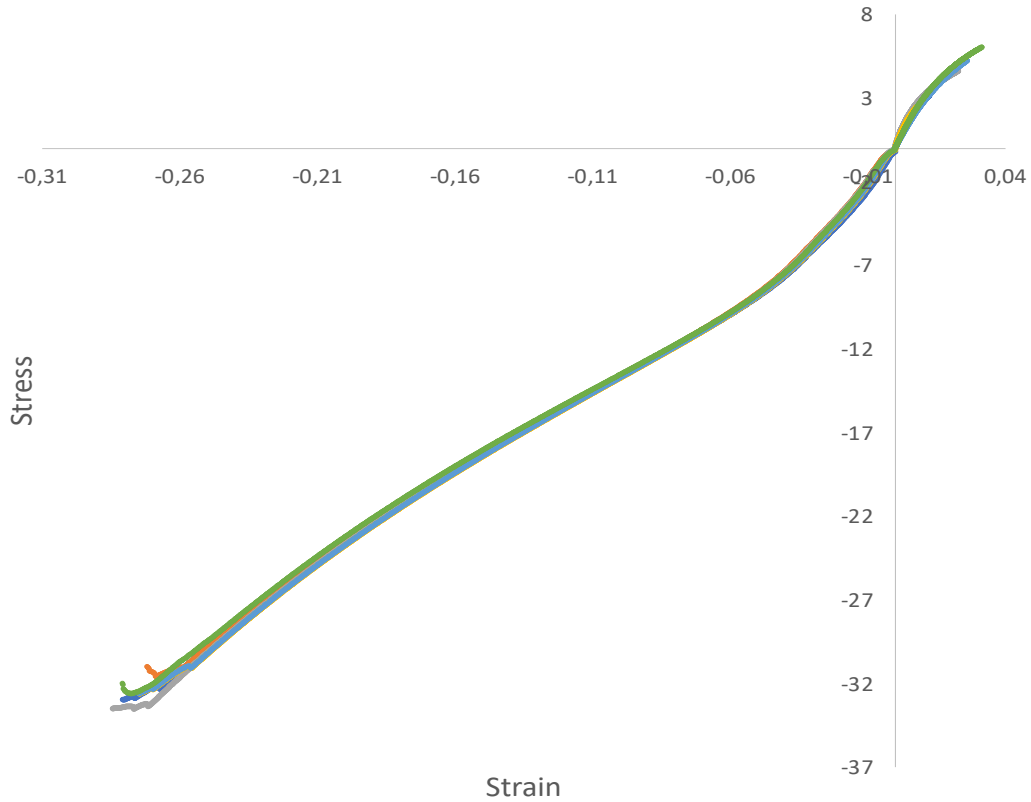

Figure 4.9: Comprehensive Stress-strain graph

4.4 SEM result

The SEM analysis gives us an image of the microstructure of the SBE, in this case, obtained by a polymer deposition on a surface that is compared with the reference microstructure of the SBE obtained by vacuum infusion [33], presented in Figure 4.10. The two images captured at the same magnitude (35k) show the same random porosity structure and the same porous length. This comparison suggests that the two microstructures are the same which means that the structure is unaffected by the type of deposition.

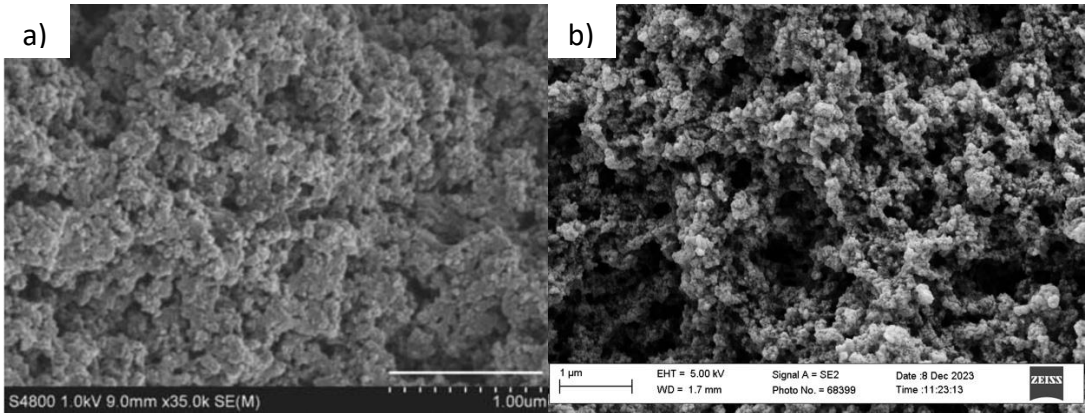

Figure 4.10: SEM images of samples obtained with different processes: a) Vacuum infusion b) Simple deposition.

4.5 Shrinkage test

After the curing process, the syringes were examined to see the possible presence of shrinkage. As Figure 4.10 shows no change in volume is remarkable, we can conclude that there are no effects of shrinkage and volume variation. This is very important because it means that we do not have the rise of stress during the curing process, so the material is stress-free once is cured.

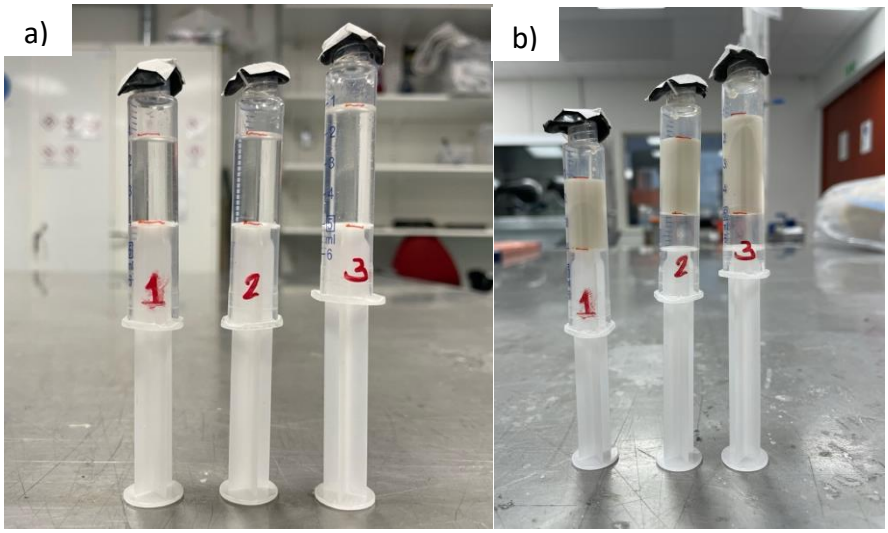

Figure 4.10: Shrinkage test, a) syringes before the curing process, b) syringes after the curing process.

4.6. FEM results

With the results we got from the test now, we can use them in the FEM model and compare the results in terms of stress with the previous Carl Larsson's work [30]. In particular, we are going to set a new Poisson ratio and Elastic Modulus for the SBE. In the following Table 8. presents the old and the new data used in the model.

Table 8. Elastic modulus and Poisson's ratio.

	OLD DATA	STUDY DATA RESULTS
ELASTIC MODULUS [MPa]	700	412
POISSON'S RATIO	0,37	0,34

The two series of data are compared using effective stress. In this case, it has been computed passing through the first Piola-Kirchhoff stress tensor as:

$$P(F) = F \cdot S(C) \quad (4.1)$$

After having been computed it, we can compute the stress components of Cauchy's stress tensor as:

$$\sigma = \frac{1}{J}[P] \cdot [F] \ (4.2)$$

After that, we can define the effective stress as $\sigma_{VM} = \sqrt{\frac{3}{2}\sum_{i,j=1}^{3} S_{ij}S_{ij}}$ (4.3) with S_{ij} refers to the deviatoric part of the stress. A comparison between the two different effective stress is shown in Figure 4.11.

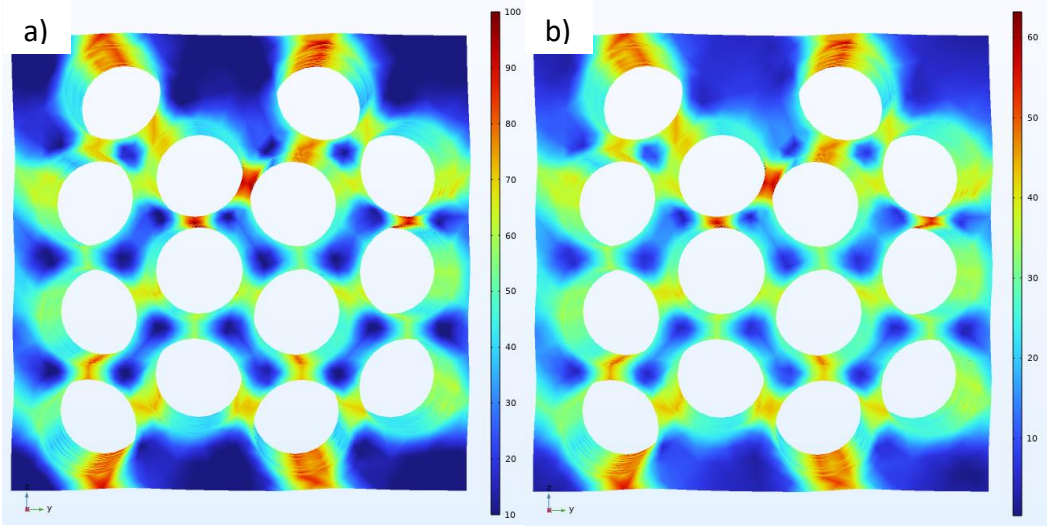

Figure 4.11: Representation of the effective stress on the unconstrained RVE in a finite strain setting, a) Previous study work b) Updated study. The periodic fluctuation solution on the boundaries u_s is shown in a magnified state.

The results show quite differences in terms of effective stress due to a different elastic modulus and Poisson's ratio, as shown in Table 9.

Table 9. Maximum and Minimum Von Mises stress results.

	OLD DATA	STUDY DATA RESULTS
$\sigma_{VM}MAX$ [MPa]	109.5	63
$\sigma_{VM}MIN$ [MPa]	0.6	0.3

This is reflected also in terms of the principal stresses, computed as:

$$\sigma_1 = \frac{I_1}{3} + \sqrt{\frac{4J_2}{3}} \cdot \cos(\theta) \quad (4.3.a)$$

$$\sigma_2 = \frac{I_1}{3} + \sqrt{\frac{4J_2}{3}} \cdot \cos\left(\theta - \frac{2\pi}{3}\right) \quad (4.3.b)$$

$$\sigma_3 = \frac{I_1}{3} + \sqrt{\frac{4J_2}{3}} \cdot \cos\left(\theta + \frac{2\pi}{3}\right) \quad (4.3.c)$$

Whit:

$$\cos(3\theta) = \frac{3\sqrt{3}}{2} \cdot \frac{J_3}{(J_2)^{3/2}} \quad (4.4)$$

Where I_1 represents the first principal stress invariant, and with J_2, and J_3 which represent the second and the third invariants of the deviatoric stress tensor.

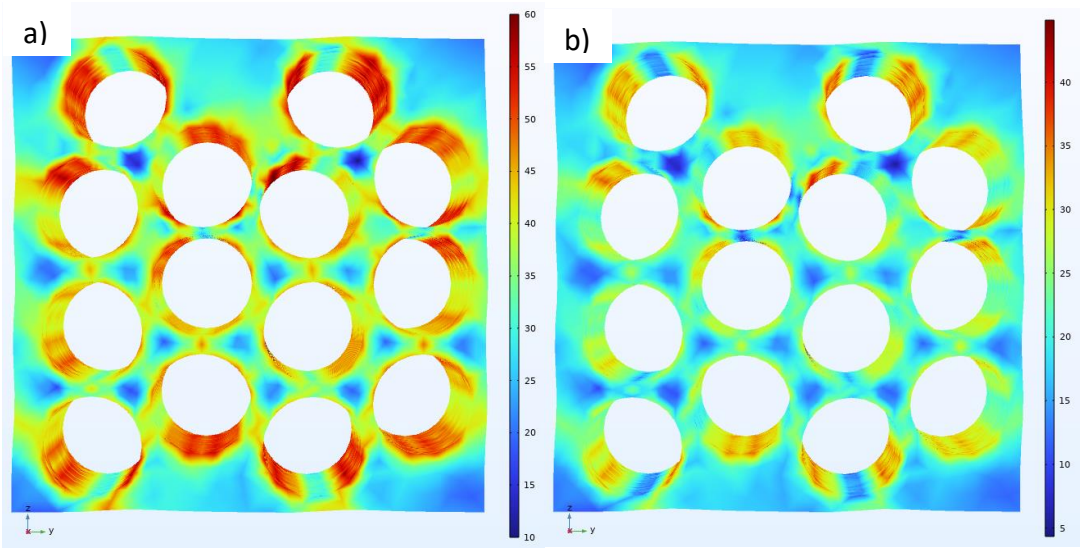

Figure 4.12: Representation of the σ_1 principal stress on the unconstrained RVE in a finite strain setting, a) Previous study work b) Updated study.

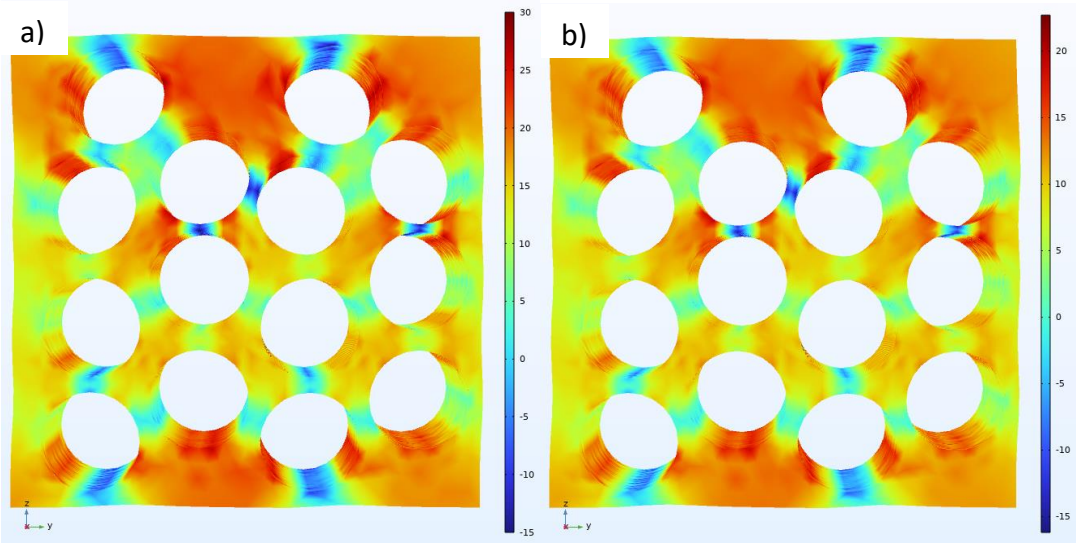

Figure 4.13: Representation of the σ_2 principal stress on the unconstrained RVE in a finite strain setting, a) Previous study work b) Updated study.

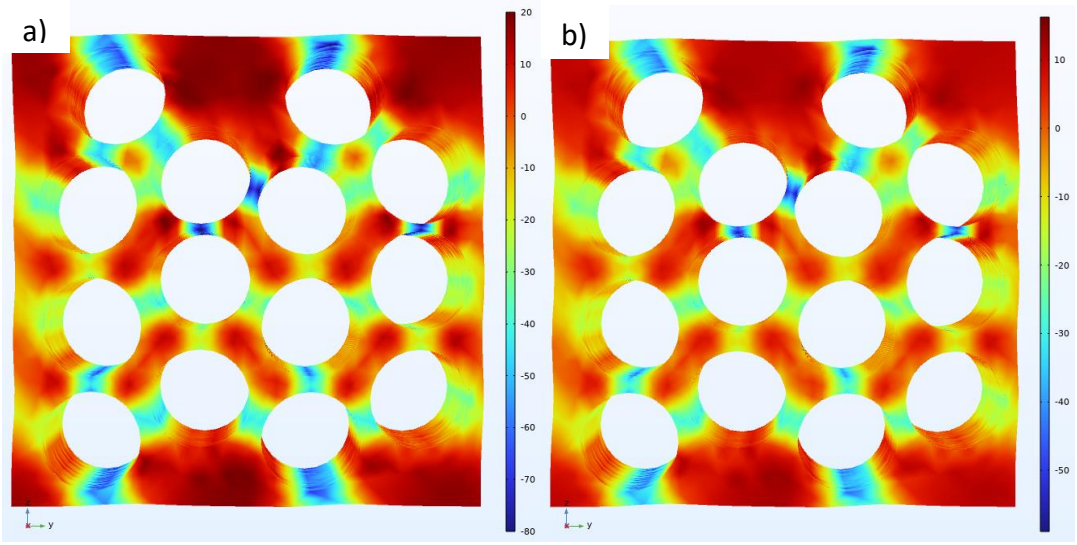

Figure 4.14: Representation of the σ_3 principal stress on the unconstrained RVE in a finite strain setting, a) Previous study work b) Updated study.

As before, differences in the absolute values of the principal stresses for the two different parameters related to the SBE are observed. Table 10. presents these differences in terms of principal stresses.

Table 10. Maximum and minimum values for each principal stress.

	OLD DATA	STUDY DATA RESULTS
$\sigma_1 MAX$[MPa]	68	45
$\sigma_1 MIN$[MPa]	8	4
$\sigma_2 MAX$[MPa]	31	23
$\sigma_2 MIN$[MPa]	-17	-16
$\sigma_3 MAX$[MPa]	23	16
$\sigma_3 MIN$[MPa]	-90	-59

At this juncture, it is crucial to assess whether the material experiences failure at its maximum state of lithiation. To address this, the evaluation employs the Raghava yield criteria as shown in equation 4.5. This choice is driven by the need to consider variations in yield stress between compression and tension, a factor not accounted for by the Von Mises yield criteria. A 2D representation of different yield criteria is illustrated in Figure 4.15.

$$\sqrt{6J_2 + 2(\sigma_{yc} - \sigma_{yt})I_1} \leq \sqrt{2\sigma_{yc}\sigma_{yt}} \quad (4.5)$$

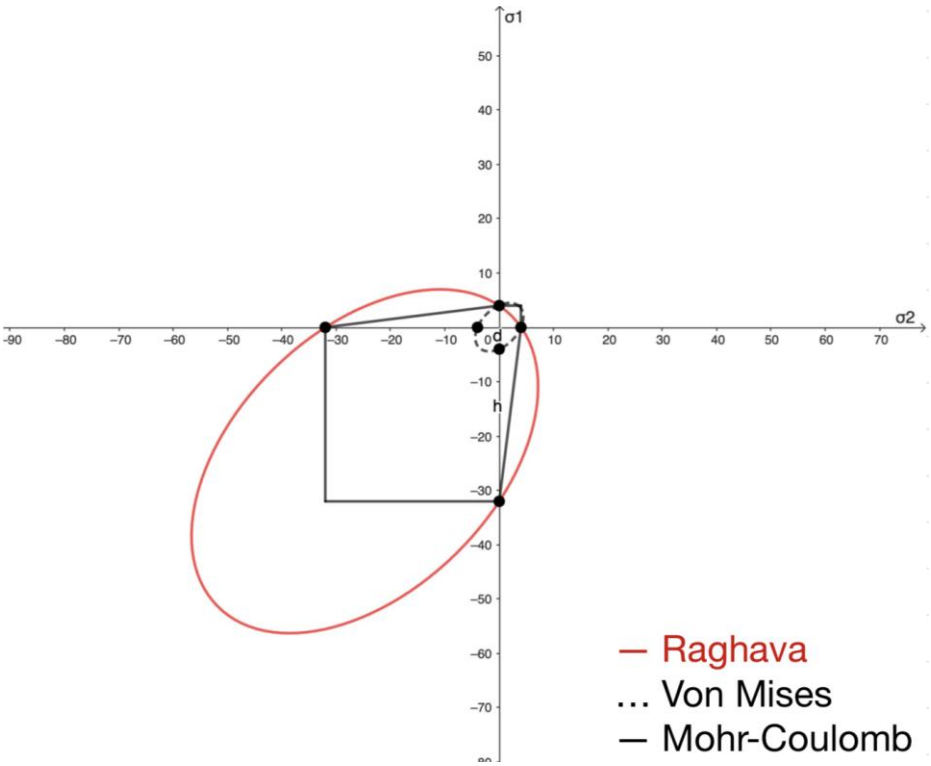

Figure 4.15: 2D representation of different yield criteria.

To compute the Raghava yield criterion, a simpler version of the RVE model is required. This is because to predict how the matrix behaves is important to know at first the material model and how the SBE behaves in terms of microscale level.
A linear elastic model and small strain are settled. Whit this setting is not possible to apply an unconstrained model because it works only with finite strain, consequentially the material undergoes high stress conditions more than how it does. But this allows us to evaluate possible critical areas that take hold during battery operation.

The effective stress and the principal stresses are computed in the following figures.

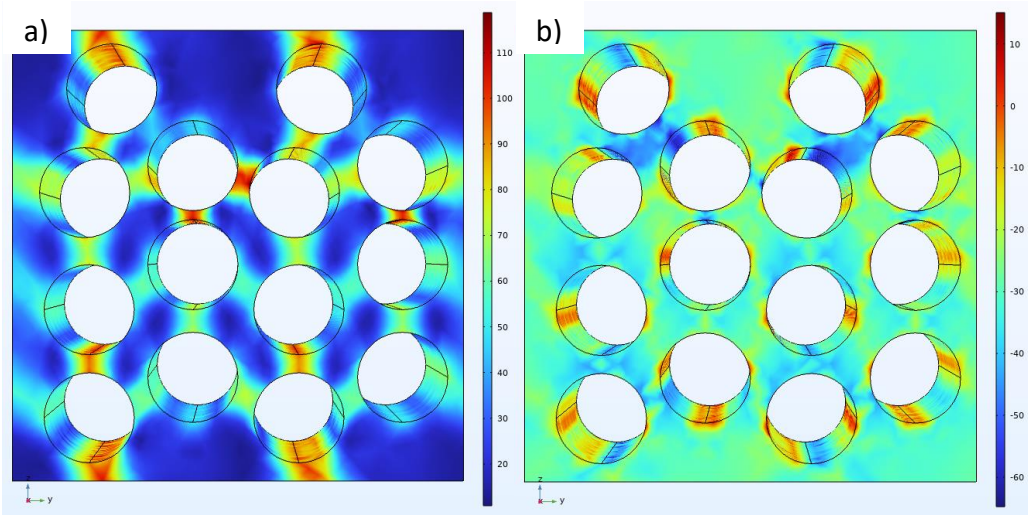

Figure 4.17: Representation of the constrained RVE in a small strain setting, a) Effective stress b) first principal stress

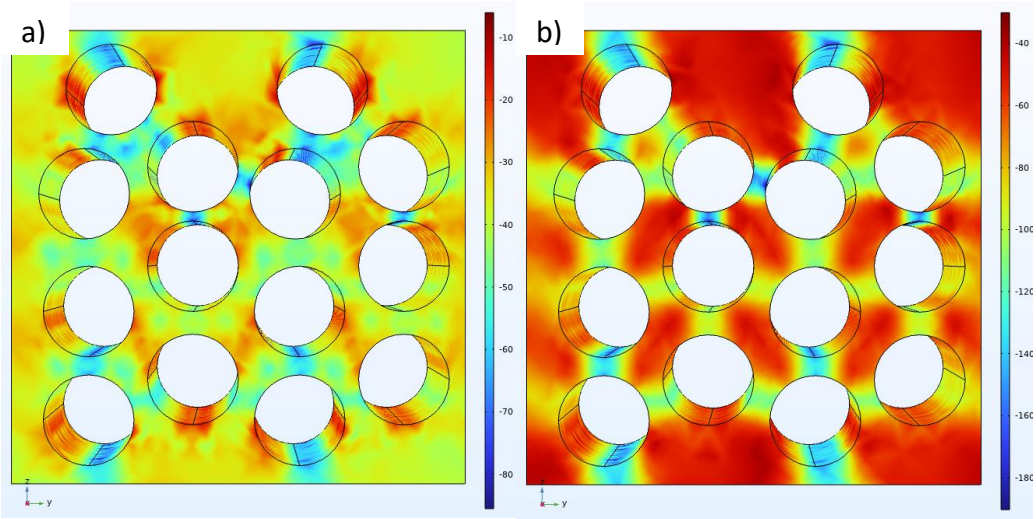

Figure 4.18: Representation of the constrained RVE in a small strain setting, a) second principal stress b) first principal stress

Table 11. Maximum and minimum ranges of stresses

$\sigma_{VM}MAX$	$\sigma_{VM}MIN$	σ_1MAX	σ_1MIN	σ_2MAX	σ_2MIN	σ_3MAX	σ_3MIN
118	10	15	-64	-6	-85	-30	-190

These results show higher values of stress compared with the unconstrained model; this is because the constraints settings do not let the material free to expand causing a higher level of stress.
At this point is important to see how the Raghava yield criterion works with a constrained model that takes into consideration only small strains.

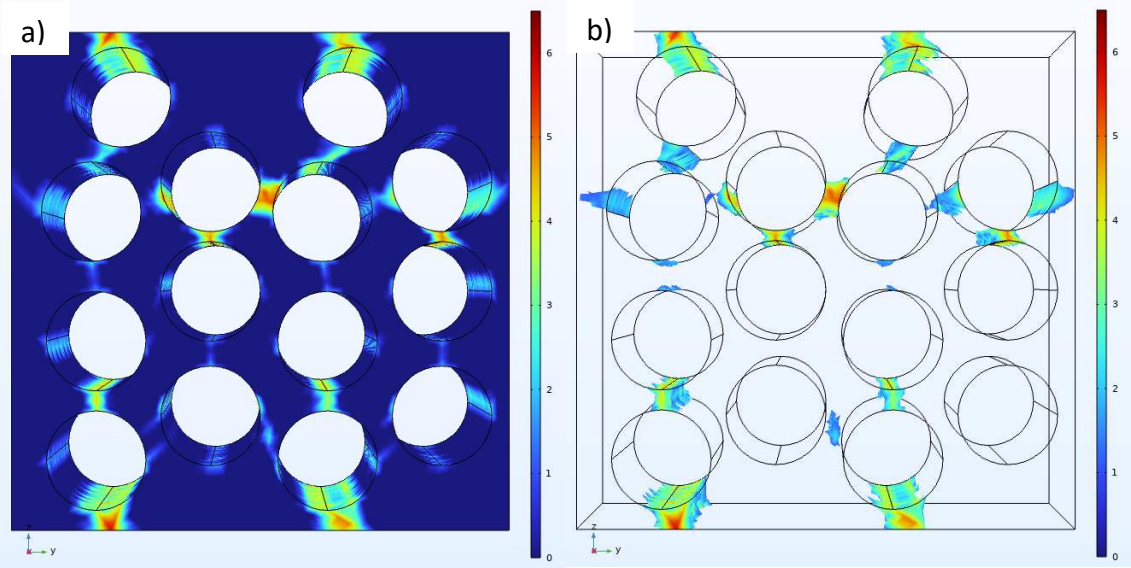

Figure 4.19: Representation of the Raghava criterion on the constrained RVE in a small strain setting. a) Raghava's full range of values b) Focus on the yielded elements.

Figure 4.19 shows that the RVE does not break overall but only in some small areas where the distance between the fibers is very close, therefore where the stress is greater. This result looks very reasonable but at the same time, we cannot take it to be perfectly true because this simple model does not represent the real behavior of the material but is just a simplified version of the previous one. It does not consider finite deformations, a non-elastic material model, and free expansion.
This analysis gives a good idea of how the SBE could be during the most critical phase of the lithiation process, i.e. when the swelling of the fiber is maximized.

After that, it has been tried to compute the Raghava yield criteria in the previous model with finite strains producing bad results as shown in Figure 4.20.

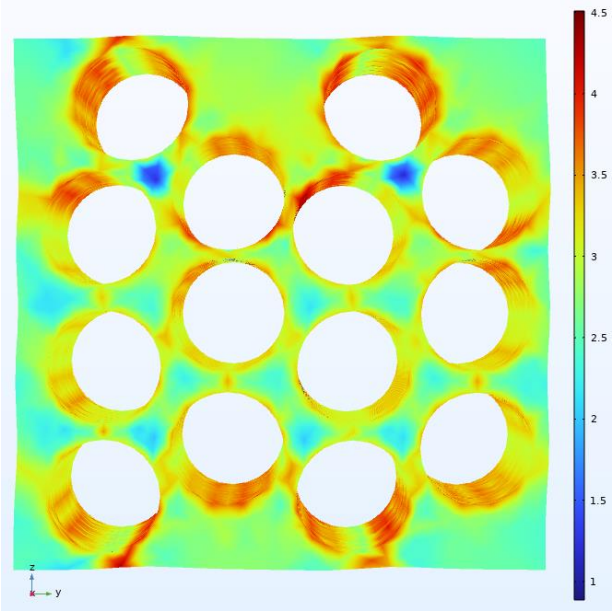

Figure 4.12: Representation of the Raghava yield criteria on the unconstrained RVE in a finite strain setting.

The given result suggests that further work is required for a more comprehensive understanding. It appears that the SBE is failing at every point of the RVE (Representative Volume Element) because each element is visualized with a value equal to or greater than 1. However, this outcome is deemed inaccurate, as in a realistic scenario, if the material were genuinely broken, it would render the component non-functional, preventing the passage of lithium through it. Such a condition would lead to a significant loss of mechanical properties in contrast to the findings presented in the work of Johanna Xu [34]. Therefore, additional investigations and refinements are necessary to reconcile these discrepancies and obtain a more accurate understanding of the system's behavior.

CONCLUSIONS

In conclusion, this thesis has successfully conducted mechanical tests to characterize the Structural Battery Element (SBE) within structural batteries. Valuable insights have been provided, offering guidelines for the production, and testing of specimens designed for mechanical tensile and compression tests. The outcomes of this research furnish essential data, enabling us to comprehend the material's behavior through general values and graphical representations depicting the stress-deformation trend.

The culmination of these efforts has allowed for an evaluation of the material's behavior within the negative electrode during a lithiation cycle. Notably, the observed swelling of the fibers has been identified as a significant factor contributing to an increase in localized stress, particularly in areas where the fibers are closely positioned. This research not only contributes to our understanding of the structural battery element but also lays the groundwork for further exploration and refinement of structural battery technology.

FUTURE WORK

The results of this study have sparked numerous inquiries, necessitating a more comprehensive comprehension of the material.

- The hyperelastic Neo-Hookean material model falls short in accurately representing the material behavior. Therefore, exploring alternative material models becomes imperative to achieve a more precise assessment of stress during lithiation and delithiation processes.

- While this work lays the groundwork for understanding the macroscopic behavior of the SBE (Structural Battery Element), a more meticulous investigation at the microscale is essential. Conducting tests such as micro-indentation can offer enhanced insights into the SBE's behavior.

- There is a crucial need to unravel the intricate interaction dynamics between fibers and matrix, encompassing factors such as adhesion, stress distribution, and load transmission.

- A microscopic examination of the matrix post-lithiation cycles, particularly through SEM (Scanning Electron Microscopy), is warranted. This observation aims to quantify the presence of voids or cracks at the matrix level near the fibers.

- A comprehensive review of the finite element model is essential to align the results with those obtained from physical tests.

Upon achieving an in-depth understanding of the material, further exploration will focus on unraveling the coupling mechanisms between the matrix and fibers, providing a holistic insight into the structural battery.

BIBLIOGRAPHY

[1] R. F. Gibson, “A review of recent research on mechanics of multifunctional composite materials and structures,” *Compos. Struct.*, vol. 92, no. 12, pp. 2793–2810, Nov. 2010, doi: 10.1016/j.compstruct.2010.05.003.

[2] T. Pereira, Z. Guo, S. Nieh, J. Arias, and H. T. Hahn, “Energy Storage Structural Composites: a Review,” *J. Compos. Mater.*, vol. 43, no. 5, pp. 549–560, Mar. 2009, doi: 10.1177/0021998308097682.

[3] S. C. Roberts and G. S. Aglietti, “Satellite multi-functional power structure: Feasibility and mass savings,” *Proc. Inst. Mech. Eng. Part G J. Aerosp. Eng.*, vol. 222, no. 1, pp. 41–51, 2008, doi: 10.1243/09544100JAERO255.

[4] J. P. Thomas and M. A. Qidwai, “Mechanical design and performance of composite multifunctional materials,” *Acta Mater.*, vol. 52, no. 8, pp. 2155–2164, May 2004, doi: 10.1016/j.actamat.2004.01.007.

[5] J. P. Thomas and M. A. Qidwai, “The design and application of multifunctional structure-battery materials systems,” *JOM*, vol. 57, no. 3, pp. 18–24, Mar. 2005, doi: 10.1007/s11837-005-0228-5.

[6] J. Thomas, S. Qidwai, W. Pogue, and G. Pham, “Multifunctional structure-battery composites for marine systems,” *J. Compos. Mater.*, vol. 47, no. 1, pp. 5–26, Jan. 2013, doi: 10.1177/0021998312460262.

[7] J. F. Snyder, R. H. Carter, and E. D. Wetzel, “Electrochemical and Mechanical Behavior in Mechanically Robust Solid Polymer Electrolytes for Use in Multifunctional Structural Batteries,” *Chem. Mater.*, vol. 19, no. 15, pp. 3793–3801, Jul. 2007, doi: 10.1021/cm070213o.

[8] P. Liu, E. Sherman, and A. Jacobsen, “Design and fabrication of multifunctional structural batteries,” *J. Power Sources*, vol. 189, no. 1, pp. 646–650, Apr. 2009, doi: 10.1016/j.jpowsour.2008.09.082.

[9] S. Ekstedt, M. Wysocki, and L. E. Asp, “Structural batteries made from fibre reinforced composites,” *Plast. Rubber Compos.*, vol. 39, no. 3–5, pp. 148–150, Jun. 2010, doi: 10.1179/174328910X12647080902259.

[10] T. Carlson, “Multifunctional composite materials : Design, manufacture and experimental characterisation,” 2013, Accessed: Oct. 30, 2023. [Online]. Available: https://urn.kb.se/resolve?urn=urn:nbn:se:ltu:diva-26038

[11] M. Yoshio, R. J. Brodd, and A. Kozawa, Eds., *Lithium-Ion Batteries: Science and Technologies*. New York, NY: Springer, 2009. doi: 10.1007/978-0-387-34445-4.

[12] D. Linden and T. B. Reddy, Eds., *Handbook of batteries*, 3. ed. in McGraw-Hill handbooks. New York, NY: McGraw-Hill, 2002.

[13] L. Asp and E. Greenhalgh, “Structural power composites,” *Compos. Sci. Technol.*, vol. 101, pp. 41–61, Sep. 2014, doi: 10.1016/j.compscitech.2014.06.020.

[14] M. H. Kjell, E. Jacques, D. Zenkert, M. Behm, and G. Lindbergh, “PAN-based carbon fiber negative electrodes for structural lithium-ion batteries,” *J. Electrochem. Soc.*, vol. 158, no. 12, pp. A1455–A1460, 2011, doi: 10.1149/2.053112jes.

[15] J.-B. Donnet and R. C. Bansal, *Carbon Fibers*. CRC Press, 1998.

[16] G. Fredi *et al.*, “Graphitic microstructure and performance of carbon fibre Li-ion structural battery electrodes,” *Multifunct. Mater.*, vol. 1, no. 1, 2018, Accessed: Oct. 30, 2023. [Online]. Available: https://urn.kb.se/resolve?urn=urn:nbn:se:kth:diva-302056
[17] M. H. Kjell, T. G. Zavalis, M. Behm, and G. Lindbergh, “Electrochemical Characterization of Lithium Intercalation Processes of PAN-Based Carbon Fibers in a Microelectrode System,” *J. Electrochem. Soc.*, vol. 160, no. 9, p. A1473, Jul. 2013, doi: 10.1149/2.054309jes.
[18] J. Hagberg, S. Leijonmarck, and G. Lindbergh, “High Precision Coulometry of Commercial PAN-Based Carbon Fibers as Electrodes in Structural Batteries,” *J. Electrochem. Soc.*, vol. 163, no. 8, p. A1790, Jun. 2016, doi: 10.1149/2.0041609jes.
[19] “Multifunctional structural battery and supercapacitor composites - PDF Free Download,” c.coek.info. Accessed: Oct. 30, 2023. [Online]. Available: https://c.coek.info/pdf-multifunctional-structural-battery-and-supercapacitor-composites-.html
[20] D. J. Johnson, “Structure-property relationships in carbon fibres,” *J. Phys. Appl. Phys.*, vol. 20, no. 3, p. 286, Mar. 1987, doi: 10.1088/0022-3727/20/3/007.
[21] V. Tu, L. E. Asp, N. Shirshova, F. Larsson, K. Runesson, and R. Jänicke, “Performance of bicontinuous structural electrolytes,” *Multifunct. Mater.*, vol. 3, no. 2, p. 025001, May 2020, doi: 10.1088/2399-7532/ab8d9b.
[22] M. S. Siraj *et al.*, “Advancing Structural Battery Composites: Robust Manufacturing for Enhanced and Consistent Multifunctional Performance,” *Adv. Energy Sustain. Res.*, vol. n/a, no. n/a, p. 2300109, doi: 10.1002/aesr.202300109.
[23] J. Snyder, E. Gienger, and E. Wetzel, “Performance metrics for structural composites with electrochemical multifunctionality,” *J. Compos. Mater.*, vol. 49, no. 15, pp. 1835–1848, Jun. 2015, doi: 10.1177/0021998314568167.
[24] E. Jacques, M. H. Kjell, D. Zenkert, G. Lindbergh, M. Behm, and M. Willgert, “Impact of electrochemical cycling on the tensile properties of carbon fibres for structural lithium-ion composite batteries,” *Compos. Sci. Technol.*, vol. 72, no. 7, pp. 792–798, Apr. 2012, doi: 10.1016/j.compscitech.2012.02.006.
[25] S. Duan *et al.*, “Three-dimensional reconstruction and computational analysis of a structural battery composite electrolyte,” *Commun. Mater.*, vol. 4, no. 1, Art. no. 1, Jun. 2023, doi: 10.1038/s43246-023-00377-0.
[26] E. Jacques, M. H. Kjell, D. Zenkert, and G. Lindbergh, “The effect of lithium-intercalation on the mechanical properties of carbon fibres,” *Carbon*, vol. 68, pp. 725–733, Mar. 2014, doi: 10.1016/j.carbon.2013.11.056.
[27] E. Jacques, M. Kjell, D. Zenkert, G. Lindbergh, and M. Behm, “Impact of mechanical loading on the electrochemical behaviour of carbon fibers for use in energy storage composite materials,” presented at the 18th International Conference on Composites Materials, ICCM 2011, 21 August 2011 through 26 August 2011, Jeju, 2011. Accessed: Oct. 30, 2023. [Online]. Available: https://urn.kb.se/resolve?urn=urn:nbn:se:kth:diva-148689
[28] L. E. Asp, M. Johansson, G. Lindbergh, J. Xu, and D. Zenkert, “Structural battery composites: a review,” *Funct. Compos. Struct.*, vol. 1, no. 4, p. 042001, Nov. 2019, doi: 10.1088/2631-6331/ab5571.
[29] L. E. Asp, L. A. Berglund, and R. Talreja, “A criterion for crack initiation in glassy

polymers subjected to a composite-like stress state," *Compos. Sci. Technol.*, vol. 56, no. 11, pp. 1291–1301, Jan. 1996, doi: 10.1016/S0266-3538(96)00090-5.
[30] C. Larsson, F. Larsson, J. Xu, K. Runesson, and L. E. Asp, "Effects of lithium insertion induced swelling of a structural battery negative electrode," *Compos. Sci. Technol.*, vol. 244, p. 110299, Nov. 2023, doi: 10.1016/j.compscitech.2023.110299.
[31] S. Duan *et al.*, "Effect of lithiation on the elastic moduli of carbon fibres," *Carbon*, vol. 185, pp. 234–241, Nov. 2021, doi: 10.1016/j.carbon.2021.09.037.
[32] D. Carlstedt *et al.*, "Experimental and computational characterization of carbon fibre based structural battery electrode laminae," *Compos. Sci. Technol.*, vol. 220, p. 109283, Mar. 2022, doi: 10.1016/j.compscitech.2022.109283.
[33] L. M. Schneider, N. Ihrner, D. Zenkert, and M. Johansson, "Bicontinuous Electrolytes via Thermally Initiated Polymerization for Structural Lithium Ion Batteries," *ACS Appl. Energy Mater.*, vol. 2, no. 6, pp. 4362–4369, Jun. 2019, doi: 10.1021/acsaem.9b00563.
[34] J. Xu *et al.*, "A multicell structural battery composite laminate," *EcoMat*, vol. 4, no. 3, p. e12180, 2022, doi: 10.1002/eom2.12180.